

Note: This work has not yet been peer-reviewed and is provided by the contributing author(s) via EarthArXiv.org as a means to ensure timely dissemination of scholarly and technical work on a noncommercial basis. Copyright and all rights therein are maintained by the author(s) or by other copyright owners. It is understood that all persons copying this information will adhere to the terms and constraints invoked by each author's copyright. This work may not be reposted without explicit permission of the copyright owner. This work is under review at the *Journal of Physical Oceanography*. Copyright in this work may be transferred without further notice.

Diapycnal motion, diffusion, and stretching of tracers in the ocean

Henri F. Drake,^{a,b} Xiaozhou Ruan,^c Raffaele Ferrari,^c

^a *Princeton University / Geophysical Fluid Dynamics Laboratory*

^b *Previously, MIT–WHOI Joint Program in Oceanography/Applied Ocean Science & Engineering, Cambridge and Woods Hole, Massachusetts.*

^c *Massachusetts Institute of Technology, Department of Earth, Atmospheric, and Planetary Sciences*

⁹ *Corresponding author:* Henri F. Drake, henrifdrake@gmail.com

10 ABSTRACT: Small-scale mixing drives the diabatic upwelling that closes the abyssal ocean
11 overturning circulation. Measurements of in-situ turbulence reveal that mixing is bottom-enhanced
12 over rough topography, implying downwelling in the interior and stronger upwelling in a sloping
13 bottom boundary layer. However, in-situ mixing estimates are indirect and the inferred vertical
14 velocities have not yet been confirmed. Purposeful releases of inert tracers, and their subsequent
15 spreading, have been used to independently infer turbulent diffusivities; however, these Tracer
16 Release Experiments (TREs) provide estimates in excess of in-situ ones. In an attempt to reconcile
17 these differences, Ruan and Ferrari (2021) derived exact buoyancy moment diagnostics, which
18 we here apply to quasi-realistic simulations. We show in a numerical simulation that tracer-
19 averaged diapycnal motion is directly driven by the tracer-averaged buoyancy velocity, a convolution
20 of the asymmetric upwelling/downwelling dipole. Diapycnal spreading, however, involves both
21 the expected contribution from the tracer-averaged in-situ diffusion and an additional non-linear
22 diapycnal stretching term. These diapycnal stretching effects, caused by correlations between
23 buoyancy and the buoyancy velocity, can either enhance or reduce tracer spreading. Diapycnal
24 stretching in the stratified interior is compensated by diapycnal contraction near the bottom; for
25 simulations of the Brazil Basin Tracer Release Experiment these nearly cancel by coincidence.
26 By contrast, a numerical tracer released near the bottom experiences leading-order stretching that
27 varies in time. These results suggest mixing estimates from TREs are not unambiguous, especially
28 near topography, and that more attention should be paid towards the evolution of tracers' first
29 moments.

30 1. Introduction

31 The lower limb of the ocean’s meridional overturning circulation traces the diabatic life cycle of
32 abyssal bottom waters (Talley 2013), which store vast quantities of climatically-active tracers like
33 heat and carbon. Bottom waters are formed at the surface of the Southern Ocean by atmospheric
34 cooling and brine rejection and are consumed in the deep ocean by buoyancy-flux convergence
35 due to small-scale mixing and geothermal heating (Abernathey et al. 2016; de Lavergne et al.
36 2016b). Since mixing processes are too small to be resolved by large-scale ocean models, the rate
37 at which tracers are mixed across density surfaces— the diapycnal diffusivity— enters as a key free
38 parameter in ocean and climate models (Bryan and Lewis 1979; Simmons et al. 2004; de Lavergne
39 et al. 2020). While early models of the abyssal circulation assume this mixing to be spatially
40 uniform (Munk 1966; Stommel and Arons 1959), subsequent in-situ observations reveal a complex
41 geography of mixing processes (e.g. Polzin et al. 1997; Waterhouse et al. 2014). A robust pattern
42 that emerges from these in-situ mixing observations is the bottom-enhancement of mixing over
43 rough topography, consistent with theoretical arguments that this mixing is predominantly caused
44 by breaking internal waves radiating from flow over topography (Munk and Wunsch 1998; Polzin
45 2009; Nikurashin and Ferrari 2009; Nikurashin and Legg 2011; MacKinnon et al. 2017; Whalen
46 et al. 2020).

47 The observed bottom-enhancement of deep mixing demands a revision of classic abyssal circu-
48 lation theory: in the stratified interior, bottom-enhanced mixing above rough topography results in
49 a layer of buoyancy flux divergence—the downwelling Stratified Mixing Layer (SML)—and a thin
50 layer of even larger buoyancy flux convergence at the insulating¹ seafloor—the upwelling Bottom
51 Boundary Layer (BBL). These ideas were first introduced as the regional scale in the Brazil Basin
52 (Polzin et al. 1997; Ledwell et al. 2000; St. Laurent et al. 2001; Huang and Jin 2002) and then
53 generalized to the global context by (Ferrari et al. 2016; McDougall and Ferrari 2017; Callies
54 and Ferrari 2018). The global diabatic overturning circulation is the small residual of substantial
55 downwelling in the SML and even larger upwelling in the BBL (Ferrari et al. 2016; Drake et al.
56 2020). While the existence of these upwelling/downwelling flows is virtually guaranteed by the
57 combination of a bottom-enhanced turbulent buoyancy flux and an insulating boundary condi-
58 tion along a sloping seafloor, their structure, magnitudes, and underlying dynamics remain poorly

¹Geothermal heat flux into the BBL acts to amplify upwelling, but is thought to be secondary to mixing globally (de Lavergne et al. 2016a) and is negligible in the Brazil Basin subregion considered here (Thurnherr et al. 2020).

59 understood (Callies 2018; Drake et al. 2020; Polzin and McDougall 2022). Since diapycnal (or
60 vertical) velocities and fluxes are challenging to measure directly due to the ocean’s small aspect
61 ratio, indirect methods must be used to infer the flow, such as volume or buoyancy budgets (e.g.
62 St. Laurent et al. 2001; Lele et al. 2021). Watermass transformation analysis is a commonly-used
63 framework which combines volume and buoyancy budgets to express diapycnal transport across a
64 buoyancy surface in terms of the average turbulent buoyancy flux along the surface, which can be
65 inferred from indirect observations (Walín 1982; Marshall et al. 1999; de Lavergne et al. 2016b;
66 Ferrari et al. 2016; Spingys et al. 2021).

67 There are several observational methods for estimating in-situ turbulent buoyancy fluxes and
68 their corresponding diffusivities (listed roughly in order of decreasing accuracy and generality;
69 Gregg et al. 2018): 1) velocity variance microstructure based on an approximate turbulent kinetic
70 energy budget (Osborn 1980), 2) temperature variance microstructure based on an approximate
71 temperature variance budget (Osborn and Cox 1972), 3) scaling analysis based on the Thorpe
72 scale of density overturns (Thorpe and Deacon 1977; Dillon 1982), and 4) shear/strain variance
73 finestructure based on idealized spectral models of internal wave dynamics (e.g. Garrett and Munk
74 1972, 1975; Henyey et al. 1986; Gregg 1989; Polzin et al. 1995; Gregg et al. 2003; Kunze et al.
75 2006). All of these methods are indirect and require some degree of approximation to convert
76 the measured quantity into a diffusivity. Furthermore, they provide only localized snapshots of
77 spatially and temporally intermittent mixing events and thus may provide biased estimates of the
78 mean diffusivity (Whalen 2021), which is often the goal of parameterization.

79 Tracer (or Dye²) Release Experiments (TREs; Watson et al. 1988) are considered by many
80 to provide the gold standard of mixing rate estimates. In TREs, an assumed inert chemical
81 tracer is deliberately injected into the ocean and its distribution is surveyed by ship-board rosette
82 sampling over timescales of months to years. The evolution of the tracer is then inverted (using
83 approximate advection-diffusion models) to yield estimates of the mean diffusivity and velocity,
84 which can be compared to independent in-situ turbulence measurements. Localized TREs are
85 experimental analogues of mathematicians’ Green’s function approach and are easier to interpret
86 than thermodynamic or biogeochemical tracers with less well known initial or boundary conditions
87 and more complicated dynamics and mixing histories (e.g. Hogg et al. 1982; Lumpkin and Speer

²Fluorescent dye can be used for timescales of hours to days and can be sampled as much higher resolution with in-situ fluorimeters (e.g. Ledwell et al. 2004), or—for near-surface releases—remote sensing instruments (Sundermeyer et al. 2007).

88 2007; Trossman et al. 2020). However, the results of the TRE inversion process still depend upon
89 the assumptions made to infer the diffusivity from simple advection-diffusion forward models.

90 Watson et al. (1988) pitch TREs in the ocean as an "unambiguous measure of the diapycnal
91 mixing rate" since tracers average over the spatial and temporal variability that challenges the
92 interpretation of in-situ mixing estimates; for example, Watson et al. (1988) hypothesize that the
93 sparse sampling of log-normally distributed (or worse, log-skew-normal) mixing events by in-situ
94 microstructure measurements risks under-estimating mean mixing rates (see also Baker and Gibson
95 1987; Cael and Mashayek 2021). Superficially, observations from two deep-ocean TREs seem to
96 corroborate this hypothesis: tracer-based estimates of mixing rates are ubiquitously 1.5–10 times
97 larger than co-located in-situ microstructure measurements (Ledwell et al. 2000; Watson et al.
98 2013; Mashayek et al. 2017). While there are ad-hoc and site-specific explanations for each of
99 these discrepancies, there is no consensus on how best to compare tracer-based and microstructure-
100 based estimates (Gregg et al. 2018), nor what to make of the fact that tracer-based estimates seem
101 to always exceed microstructure-based estimates.

102 Recent advances in the numerical modelling and theory of TREs provide some guidance for
103 interpreting tracer-based estimates of mixing and comparing them to microstructure-based esti-
104 mates. For example, Mashayek et al. (2017) use a realistic regional simulation to argue that the
105 mixing inferred from the DIMES TRE (Watson et al. 2013) was an order-of-magnitude larger than
106 the in-situ diffusivity estimated from microstructure because the average diapycnal spreading of
107 the tracer was dominated by a small fraction the tracer distribution that resided in regions of strong
108 mixing near rough topography. Ruan and Ferrari (2021) derive exact evolution equations for the
109 first and second tracer-weighted buoyancy moments (see Section 2a), which confirm Mashayek
110 et al. (2017)'s speculation that the tracer's diapycnal variance grows like the tracer-weighted in-situ
111 diffusivity. Ruan and Ferrari (2021) also identify a second "diapycnal stretching" term through
112 which the bottom-enhancement of the buoyancy velocity in the SML further accelerates the diapy-
113 cnal spreading of the tracer. Holmes et al. (2019) use a similar approach but include the effects
114 of a sloping bottom boundary, and find that the diapycnal stretching in the SML is somewhat
115 compensated for by a diapycnal contraction (or "boundary suppression") effect due to upwelling of
116 relatively dense tracer in the BBL. However, since both of these analyses use extremely idealized
117 models, it remains unclear to what extent diapycnal stretching affects tracers in realistic conditions.

118 Previous studies have speculated about the qualitative impacts of these stretching effects (Ledwell
 119 and Hickey 1995; Ledwell et al. 2000; Waterman et al. 2013), but did not quantify these impacts
 120 or the degree to which stretching effects are even included in their inverse models.

121 In this paper, we apply the buoyancy moments method in a quasi-realistic TRE simulation. We
 122 use tracer-weighted buoyancy moments diagnosed from the simulation to reinterpret the diapycnal
 123 downwelling and spreading observed in the Brazil Basin TRE (BBTRE; Ledwell et al. 2000 and
 124 St. Laurent et al. 2001) in the context of an emerging paradigm of bottom mixing layer control
 125 of the global abyssal circulation (Ferrari et al. 2016; McDougall and Ferrari 2017). We also
 126 provide guidance for the interpretation of past (e.g. Ledwell and Hickey 1995; Ledwell et al. 2004;
 127 Holtermann et al. 2012; Ledwell et al. 2016; Mackay et al. 2018; Visbeck et al. 2020) and future
 128 TREs that encounter topography.

129 2. Theory

130 We briefly review Ruan and Ferrari (2021)'s recently proposed framework for comparing tracer-
 131 based and microstructure-based mixing estimates, based on exact evolution equations for tracer
 132 moments in buoyancy space. The derivation begins with the conservation equations for tracer
 133 concentration c and buoyancy b ,

$$\frac{\partial c}{\partial t} + \mathbf{u} \cdot \nabla c = \nabla \cdot (\kappa \nabla c) \quad (1)$$

$$\frac{\partial b}{\partial t} + \mathbf{u} \cdot \nabla b = \nabla \cdot (\kappa \nabla b), \quad (2)$$

134 where \mathbf{u} is the velocity vector, $\nabla = \left(\frac{\partial}{\partial x}, \frac{\partial}{\partial y}, \frac{\partial}{\partial z} \right)$ is the gradient operator, and κ is an isotropic
 135 turbulent diffusivity (assumed to be the same for all tracers). Buoyancy, tracer concentrations,
 136 and velocity have been filtered on spatial and temporal scales larger than those associated with
 137 small-scale turbulence, and the filtered scalar fluxes are parameterized as an enhanced diffusive flux
 138 $\mathbf{F}_\phi = -\kappa \nabla \phi$, where the effective turbulent diffusivity is much larger than the molecular diffusivity.
 139 For simplicity of exposition, we here approximate density as a linear function of temperature; thus,
 140 density ρ , buoyancy b , and temperature T are all proportional and will be used interchangeably
 141 throughout: $b \equiv -g \frac{\rho}{\rho_0} \approx g \alpha T$, where ρ_0 is a reference density and α is the thermal contraction

142 coefficient. (Salinity can be easily included as long as it is assumed to also be linearly proportional
 143 to density.)

144 *a. Exact tracer-weighted buoyancy-moment models*

145 In his classic paper, Taylor (1922) demonstrates that the growth rate of half the second moment
 146 of a 1D tracer distribution in physical space is exactly equal to its diffusivity. Ruan and Ferrari
 147 (2021) generalize this theory to the case of variable diffusivity in a stably stratified fluid by
 148 considering moments in buoyancy space. By cross-multiplying the passive tracer (1) and buoyancy
 149 (2) equations and integrating over a volume \mathcal{V} containing the tracer (or bounded by insulating and
 150 impermeable boundaries), they derive straightforward and exact evolution equations for the first
 151 and second tracer-weighted buoyancy moments,

$$w_{\text{tracer}} \equiv \frac{\overline{\partial_t \bar{T}}}{|\nabla T|} = \frac{2\bar{\omega}}{|\nabla T|} \quad \text{and} \quad (3)$$

152

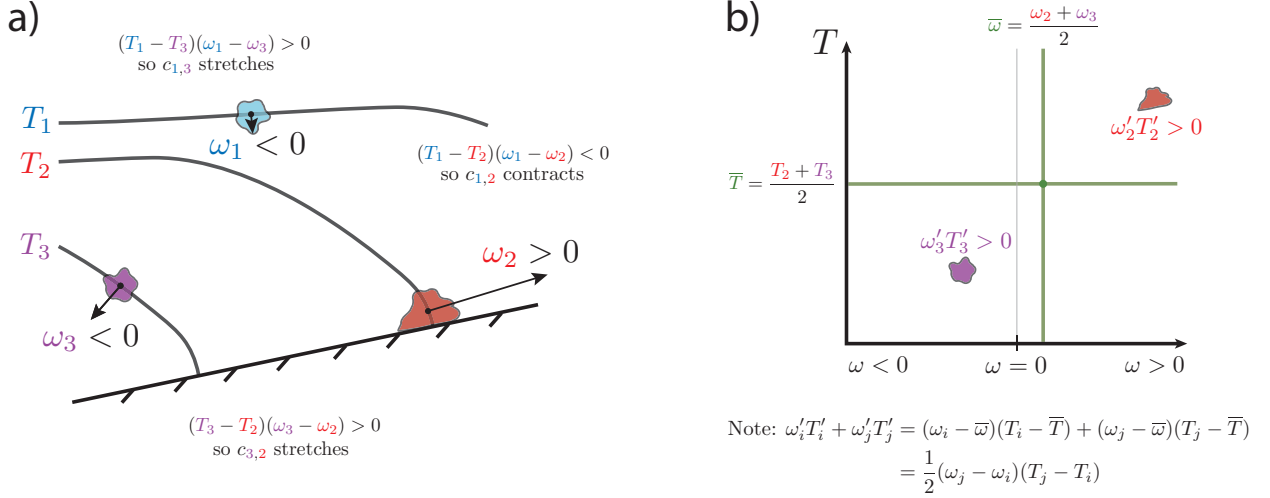
$$\underbrace{\frac{1}{2} \frac{\overline{\partial_t (T - \bar{T})^2}}{|\nabla T|^2}}_{\substack{\kappa_{\text{tracer}} \\ \text{(spreading)}}} = \underbrace{\frac{\overline{\kappa |\nabla T|^2}}{|\nabla T|^2}}_{\substack{\kappa_{\text{Taylor}} \\ \text{(diffusion)}}} + 2 \underbrace{\frac{\overline{\omega' T'}}{|\nabla T|^2}}_{\substack{\kappa_{\omega} \\ \text{(stretching)}}, \quad (4)$$

153 respectively, where overlines denote the tracer-weighted average, $\overline{\star} \equiv \frac{\int_{\mathcal{V}} \star c dV}{\int_{\mathcal{V}} c dV}$; primes denote
 154 variations from the tracer average, $\star' \equiv \star - \overline{\star}$; and $\omega \equiv \nabla \cdot (\kappa \nabla T)$ is the in-situ buoyancy velocity,
 155 which is the magnitude of the diapycnal velocity through buoyancy space (e.g. Marshall et al.
 156 1999). We have taken an additional step of converting to physical velocity and diffusivity units by
 157 normalizing by the appropriate tracer-weighted powers of the buoyancy gradient.

165 *b. Interpreting the tracer-weighted buoyancy moments*

166 Consider the extreme example of a tracer distribution $c_{i,j}$ consisting of two infinitesimal patches
 167 at locations \mathbf{x}_i and \mathbf{x}_j and with equal mass,

$$c_{i,j}(\mathbf{x}) = \delta(\mathbf{x}_i) + \delta(\mathbf{x}_j), \quad (5)$$



158 FIG. 1. Examples of diapycnal stretching and contraction of bi-modal tracer distributions (eq. 5) in physical
 159 space (a) and in (ω, T) space (b). a) The three tracer distributions $c_{1,3}$, $c_{1,2}$, and $c_{3,2}$ experience diapycnal
 160 spreading or contraction effects due to temperature and buoyancy velocity differences. Gray lines show the
 161 equally-spaced temperature surfaces corresponding to the three tracer patches. Arrows represent the magnitude
 162 of the buoyancy velocity ω and are oriented normal to temperature surfaces. b) PDF of contributions to $c_{3,2}$'s net
 163 diapycnal stretching effects both tracer patches. Olive lines mark the average buoyancy velocity and temperature
 164 of the tracer.

168 where $\delta(\mathbf{x})$ is the Delta function. The evolution of the first moment (3) is simply given by the twice
 169 the average buoyancy velocity of the two patches,

$$\partial_t \bar{T} = 2\bar{\omega} = \omega_i + \omega_j, \quad (6)$$

170 where we use the shorthand $\phi_k \equiv \phi(\mathbf{x}_k)$. The evolution of the centered second moment (4), is given
 171 by

$$\frac{1}{2} \partial_t \overline{(T - \bar{T})^2} = \overline{\kappa |\nabla T|^2} + \frac{1}{2} \Delta \omega \Delta T, \quad (7)$$

172 where $\Delta \omega \equiv \omega_j - \omega_i$ and $\Delta T \equiv T_j - T_i$ are buoyancy velocity and temperature differences between
 173 the two patches, respectively. While the first moment tendency is simply given by the average of the
 174 two patches' tendencies, the centered second moment tendency includes an additional non-linear
 175 interaction term. If the warmer patch upwells faster than the colder patch ($\Delta \omega \Delta T > 0$), this term

176 drives diapycnal stretching (e.g. $c_{1,3}$ and $c_{3,2}$ in Figure 1); conversely, $\Delta\omega\Delta T < 0$ corresponds to
 177 diapycnal contraction (e.g. $c_{1,2}$ in Figure 1).

178 A corollary of (7) is the fact that estimates of the in-situ diffusivity are most reliable when the
 179 injected tracer distribution is compact in buoyancy space (i.e. $\Delta T \approx 0$), supporting the practice
 180 of localized TREs. Even for an initially compact tracer injection with $\Delta\omega\Delta T \simeq 0$, diapycnal
 181 stretching effects may become significant over time as ΔT increases due to diapycnal diffusion; on
 182 the other hand, while isopycnal stirring does not increase ΔT (by definition), it can increase $\Delta\omega$ by
 183 distributing tracer into regions with varying buoyancy velocities. While the former effect is likely
 184 to be well represented in 1D advection-diffusion models used to interpret TRE data, the latter is
 185 not.

186 3. Numerical methods overview: simulated Tracer Release Experiments

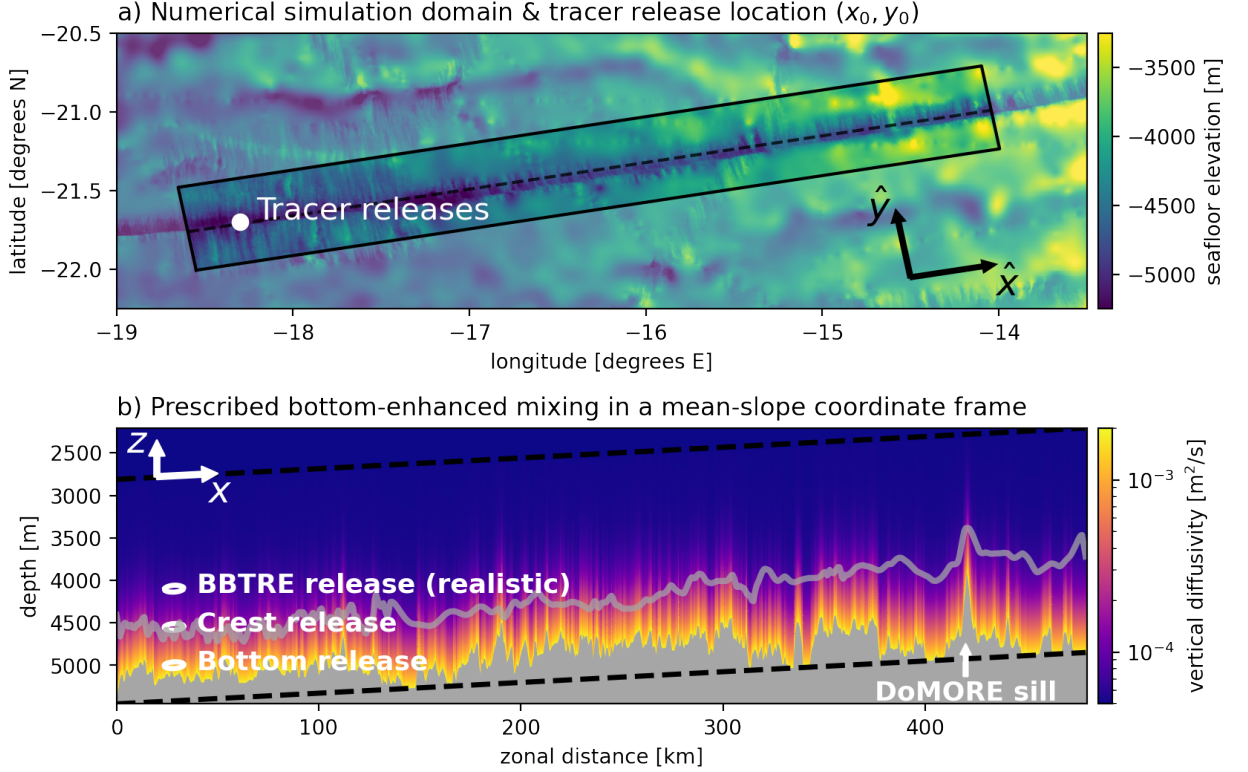
195 We configure the MITgcm to simulate mixing-driven flow in the BBTRE region (Figure 2a).
 196 Inspired by sloping bottom boundary layer theory (reviewed by Garrett et al. 1993), the system is
 197 solved in a coordinate frame aligned with the mean MAR slope, as described in detail in a submitted
 198 companion manuscript (Drake et al. 2022) and summarized in Appendix A. The simulation is forced
 199 only by bottom-enhanced turbulent mixing, which controls diabatic tracer upwelling and spreading
 200 and is thought to provide much of the available potential energy that drives sub-inertial abyssal
 201 flows. Sub-grid scale turbulent fluxes of a filtered tracer ϕ are parameterized as down-gradient
 202 turbulent diffusion, $\mathbf{F}_\phi \approx -\kappa\nabla\phi$, whose magnitude is controlled by a turbulent diffusivity κ that
 203 increases exponentially towards the seafloor (Figure 2b),

$$\kappa(x, y, z) = \kappa(z; d) = \kappa_{\text{BG}} + \kappa_{\text{BOT}} \exp\left(\frac{z-d}{h}\right),$$

204 and is fit to the mean height-above-bottom microstructure profile in the region according to Callies
 205 (2018), with $\kappa_{\text{BOT}} = 1.8 \times 10^{-3} \text{ m}^2/\text{s}$, $\kappa_{\text{BG}} = 5.2 \times 10^{-5} \text{ m}^2/\text{s}$, and $h = 230 \text{ m}$.

206 After spinning up the flow to a quasi-equilibrium state at $t = 5000$ days, we release three Gaussian
 207 blobs of tracer,

$$c_n(x, y, z, t = 0) = c_0 \exp\left\{-\left(\frac{(x-x_0)^2}{\sigma_x^2} + \frac{(y-y_0)^2}{\sigma_y^2} + \frac{(z-z_n)^2}{\sigma_z^2}\right)\right\}, \quad (8)$$



187 FIG. 2. Numerical model configuration: domain geometry, prescribed forcing, and key features. a) Rectangular
 188 domain (solid lines) centered along the BBTRE canyon thalweg (dashed line) and interpolated onto locally-
 189 tangent cartesian coordinates (\hat{x}, \hat{y}) . b) Prescribed bottom-enhanced mixing (colors) along the canyon thalweg
 190 (grey shading). Dashed black lines show the domain limits in the slope-native coordinate frame (x, z) . The
 191 transparent grey line shows the average height of the canyon crests, which rise 500 m to 1000 m above the thalweg
 192 (its deepest section). White dots/contours show the locations of the simulated tracer releases. The location of
 193 the prominent Dynamics of the Mid-Ocean Ridge Experiment (DoMORE– see Clément et al. 2017) sill is shown
 194 for reference.

208 with horizontal widths of $\sigma_x = \sigma_y = 10$ km, a thickness $\sigma_z = 100$ m, and horizontal release co-
 209 ordinates (x_0, y_0) corresponding to the location where the tracer was released in the BBTRE
 210 ($18.3^\circ\text{W}, 21.7^\circ\text{S}$) (Figure 2). The tracers are released at three different heights z_n corresponding
 211 to distinct dynamically interesting regimes: far above the topography, $z_{\text{BBTRE}} - d(x_0, y_0) = 1050$ m
 212 above the seafloor (actual BBTRE release location; hereafter the BBTRE tracer); roughly at the
 213 height of the canyon crests, $z_{\text{Crest}} - d(x_0, y_0) = 600$ m (Crest); and within the thick BBL of the
 214 canyon trough, $z_{\text{Bottom}} - d(x_0, y_0) = 150$ m (Bottom). We follow the evolution of these released

215 tracers until $t_f = 440$ days after release, roughly corresponding to the first survey in the BBTRE at
216 14 months.

217 **4. Results**

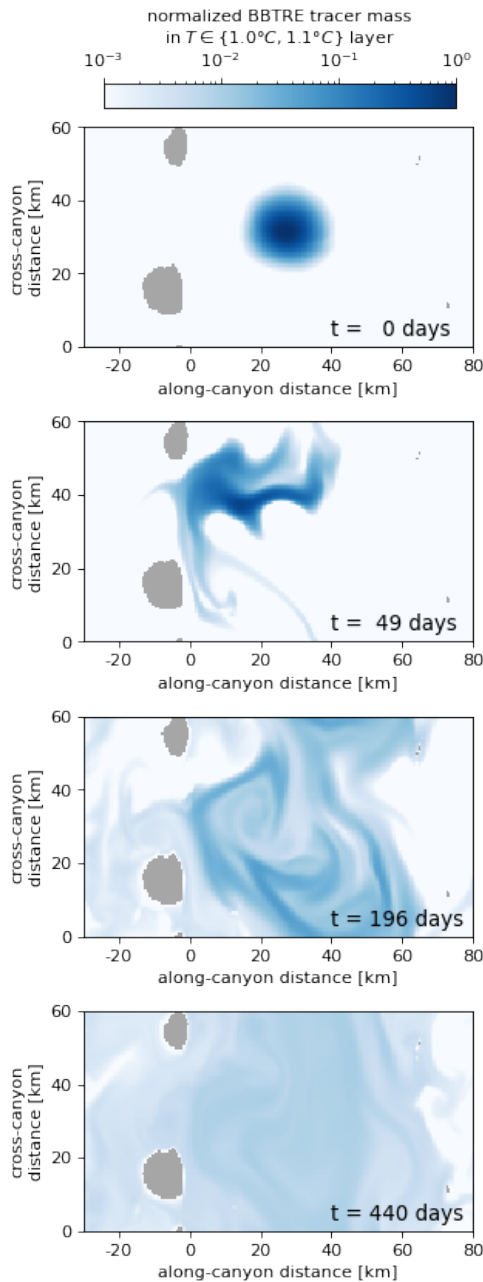
218 *a. Temporal evolution of the released tracer distributions*

222 Within the first few eddy turnover timescales, the released tracer blobs are stirred into a web
223 of filaments along isopycnals by submesoscale eddies (e.g. Figure 3). While the BBTRE and
224 Crest tracers are released well above the canyon thalweg (its deepest section; Figure 2a), vigorous
225 along-ridge mean flow (Figure 4) and isopycnal stirring by submesoscale eddies spread them to
226 shallower regions (Figure 5).

230 The tracers are diffused diapycnally by the prescribed bottom-enhanced turbulent mixing (e.g.
231 Figure 5b,d). For the BBTRE tracer, which mostly remains well above the bottom, its distribution
232 in temperature space remains reasonably Gaussian (Figure 5d), reminiscent of diffusion with a
233 constant diffusivity and in the absence of boundaries; for the Crest and Bottom tracers, however, the
234 tracer distributions depart significantly from Gaussianity (Figure 5h,l), suggesting the importance
235 of variations in the diffusivity or boundary effects. Most notably, the Bottom tracer develops a bi-
236 modal distribution in temperature space as some of the tracer spills over the minor sill at $x = 120$ km
237 and crosses the $T = 0.7^\circ\text{C}$ surface (Figure 5j, l). By the end of the experiment at 440 days, most
238 of the Bottom tracer has spilled over the sill and its bi-modal distribution collapses onto a single,
239 warmer, peak. While only the Bottom tracer exhibits a tracer-weighted diapycnal motion that is
240 discernible by visually inspecting the tracer distributions in temperature space, the BBTRE and
241 Crest tracers do exhibit slow mean diapycnal downwelling and upwelling, respectively.

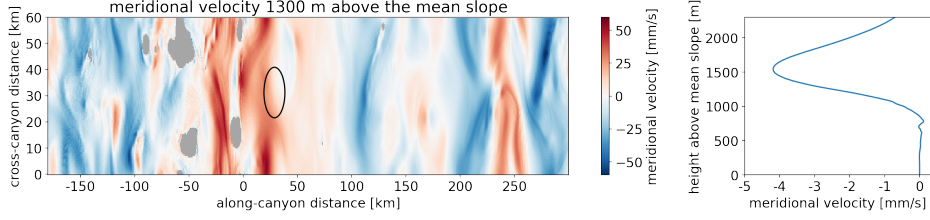
242 *b. Diapycnal interior downwelling and boundary upwelling driven by bottom-enhanced mixing*

251 As described in Section 2a, the mean diapycnal motion of the tracer is directly driven by the
252 tracer-weighted buoyancy velocity $\bar{\omega} \equiv \overline{\nabla \cdot (\kappa \nabla T)}$ (eq. 3). In the SML, well above the seafloor, the
253 bottom-enhancement of the diffusivity κ dominates the buoyancy velocity, resulting in diapycnal
254 downwelling, $\omega < 0$. Closer to the seafloor, the temperature flux must vanish to satisfy the insulating
255 bottom boundary condition, resulting in vigorous diapycnal upwelling, $\omega > 0$, in the BBL.



219 FIG. 3. Instantaneous snapshots of the BBTRE tracer mass, vertically-integrated over the $\{1.0^\circ\text{C}, 1.1^\circ\text{C}\}$
 220 temperature layer, and normalized by the maximum initial tracer mass. The grey shading represents two major
 221 topographic obstacles, where the temperature layer in-crops.

256 The BBTRE tracer, which is released in the SML, exhibits diapycnal downwelling throughout the
 257 experiment (Figure 6c), consistent with the above phenomenology. The magnitude of downwelling,
 258 however, is modulated by a 45-day damped oscillation due to along-ridge advection by a mean-flow



227 FIG. 4. (a) Cross-canyon meridional velocity 1300 m above the mean slope, i.e. at the release height of BBTRE
 228 tracer. The black contour shows the initial extent of the tracers, which is released in an anomalously northward
 229 flow. (b) Same as a), but averaged across the whole domain.

259 of speed $U \approx 15$ mm/s (Figure 4a) across a periodic domain of width $L_y = 60$ km, such that the
 260 tracer aliases the roughly sinusoidal trough-crest topography on a timescale of $\tau = L_y/U \approx 45$ days.
 261 This modulation is damped over time as the tracer spreads isopycnally and spans a region wider
 262 than the typical trough-crest separation (Figure 5a).

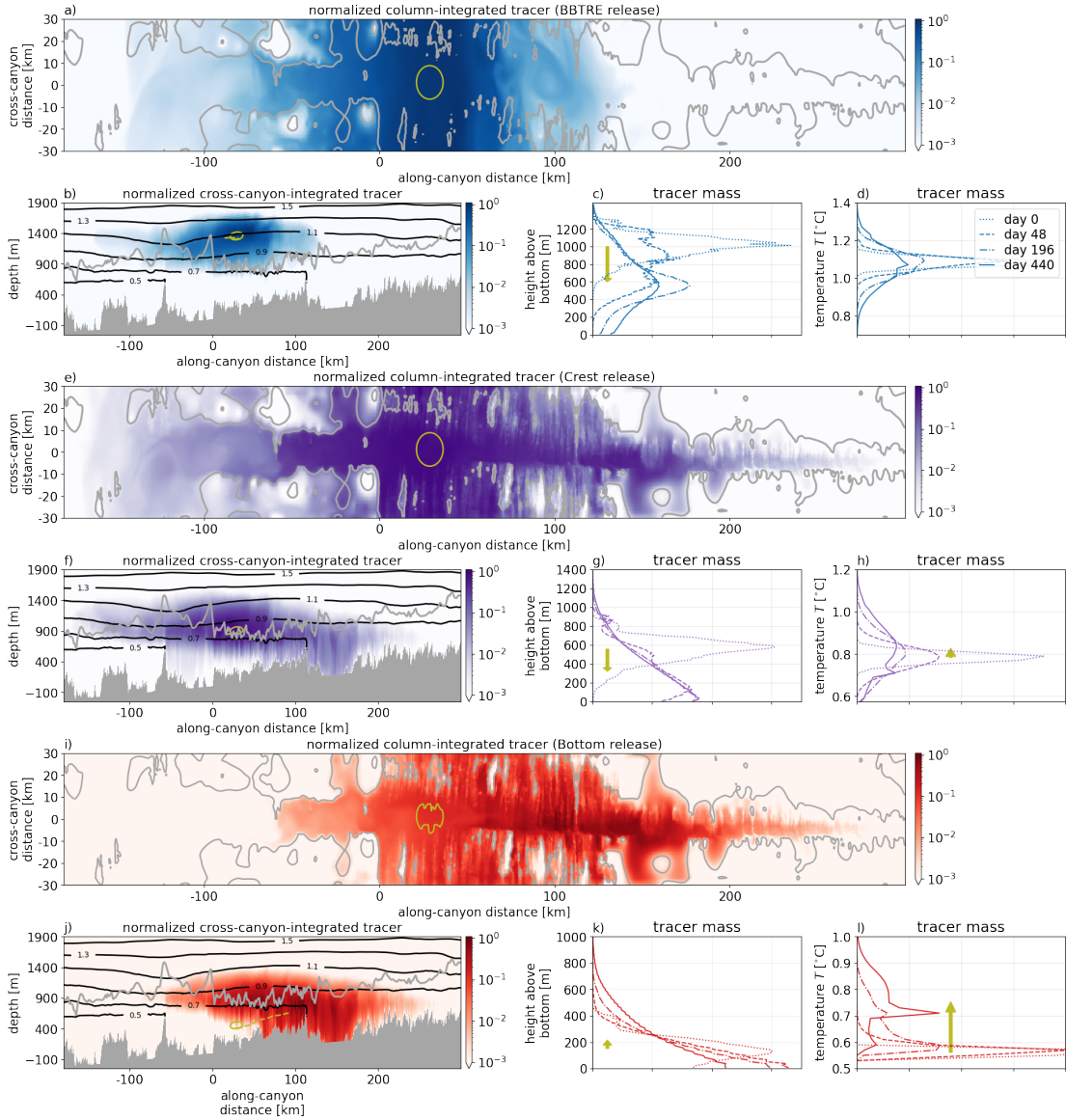
263 In the first 100 days, interpreting the mean diapycnal sinking of the BBTRE tracer is straight-
 264 forward: the entire tracer distribution experiences a negative buoyancy velocity and so the tracer
 265 sinks diapycnally (Figure 6c), i.e. $\bar{\omega} \approx \overline{\omega_{<0}}$, where we define:

$$\overline{\omega_{<0}} \equiv \frac{\int_{\mathcal{V}_{\omega < 0}} \omega c \, dV}{\int_{\mathcal{V}} c \, dV} \quad (9)$$

266 as the strictly downwelling buoyancy velocity. While this strictly downwelling contribution to the
 267 tracer-weighted buoyancy velocity increases slightly over the remainder of the experiment as the
 268 tracer sinks towards larger diffusivities, sufficient tracer is entrained into the BBL that a strictly
 269 upwelling contribution $\overline{\omega_{>0}}$ (similarly defined) grows at an even faster rate, such that the net
 270 diapycnal sinking of the tracer weakens over the last few hundred days of the experiment (Figure
 271 6c).

286 At the other extreme, the Bottom tracer is released entirely in the BBL and thus upwells vigorously
 287 upon release, with $\bar{\omega} \approx \overline{\omega_{>0}}$ (Figure 6g). As some of the tracer eventually spreads into the SML
 288 above and the strictly negative contribution $\overline{\omega_{<0}}$ grows, the net upwelling of the tracer weakens
 289 over time³.

³The Bottom tracer is released near the bottom of a weakly stratified depression along the canyon thalweg, and its average stratification increases dramatically over the first 200 days (Figure 6a,b). Thus, the early diapycnal upwelling and spreading is enhanced when converting to physical space because the buoyancy surfaces are on average much further apart than they are later on (see normalization in equations 3 and 4).



243 FIG. 5. Temporal evolution of the tracer distributions in Cartesian, height-above-bottom, and temperature
 244 coordinates for the BBTRE (a-d; blues), Crest (e-h; purples), and Bottom releases (i-l; reds). (a,e,i) Slope-normal
 245 column-integrated tracer concentrations and (b,f,j) cross-canyon-integrated tracer concentrations, normalized by
 246 their maximum value (logarithmic scale). Grey contours in (a,e,f) show two representative isobaths of ocean
 247 depth $\hat{d}(\hat{x}, \hat{y})$. Black lines in (b,f,j) show equally-spaced cross-canyon-averaged temperature surfaces. Tracer
 248 distributions in (c,g,k) height-above-bottom and (d,h,l) temperature coordinates, normalized by their maximum
 249 initial values (linear scale). Olive contours show the 10% contour for the initial tracer distribution; olive dashed
 250 and arrows show the temporal evolution of the tracer's center of mass (first moments).

290 The Crest release is perhaps the most interesting: at first, the Crest tracer is in the SML far above
 291 the canyon thalweg and thus downwells similarly to the BBTRE tracer; after roughly $\tau = 46$ days,
 292 however, enough of the Crest tracer is advected into the BBLs along the rim of the canyon and the
 293 surrounding hills that the strictly upwelling component wins out and the tracer begins upwelling
 294 in the net (Figure 6e). Over the last few hundred days of the experiment, the weak net upwelling of
 295 the tracer is the small residual of a substantial compensation between strictly upwelling and strictly
 296 downwelling contributions.

303 By plotting the evolution of the temperature moment tendency as a function of the tracer-weighted
 304 height-above-bottom, we gain a qualitative sense of the height-above-bottom structure of the in-situ
 305 buoyancy velocity (Figure 7a). As the three tracers' centers of mass drift over time, their average
 306 buoyancy velocities trace out a diapycnal downwelling that increases rapidly towards the bottom in
 307 the SML (Figure 7a, blue). Below about 300 m, however, this downwelling gives way to upwelling
 308 (Figure 7a, purple) which intensifies the closer the tracer is to the bottom (Figure 7a, red).

309 In practice, however, *instantaneous* measurement of the tracer-weighted temperature (or tem-
 310 perature variance) tendency is infeasible. Instead, practical methods are akin to estimating the
 311 time-average of the right hand-side of eq. 3 (or eq. 4) from finite differencing of the tracer-weighted
 312 volume-averaged temperature (or temperature variance)

$$\frac{1}{t_1 - t_0} \int_{t_0}^{t_1} \partial_t \bar{T} dt = \frac{\bar{T}(t_1) - \bar{T}(t_0)}{t_1 - t_0} = \frac{1}{t_1 - t_0} \int_{t_0}^{t_1} 2\bar{\omega} dt \quad (10)$$

313 between observational surveys at t_0 and t_1 , typically representing two separate cruises separated
 314 by multiple months⁴ (Watson et al. 2013; Ledwell et al. 2000). Alternatively, a linear fit through
 315 multiple surveys of $\bar{T}(t)$ can be interpreted as an estimate of *twice* the time-mean tracer-weighted
 316 buoyancy velocity. Ledwell et al. (1998) follow this general approach but incorrectly omit the
 317 factor of two, which would have brought their tracer-based mixing estimates more in-line with
 318 St. Laurent and Schmitt's (1999) in-situ mixing estimates).

319 Taking t_0 at release and $t_1 = 14$ months, as in BBTRE, the changes in the tracers' first moments
 320 still reveal the structure of abyssal mixing layer transformations, albeit at very low resolution: slow

⁴With this method, the number of distinct time-mean buoyancy velocity estimates produced by all pairs of the n surveys of $\bar{T}(t_n)$ is $\binom{n}{2} = \frac{n!}{2(n-2)!} = \frac{n(n-1)}{2} \propto n^2$, potentially providing insight into the temporal variability of mixing rates on various timescales. However, most past studies typically only consider either the n pairs that include the release as one endpoint (e.g. Watson et al.'s 2013 estimates of the second moments) or the n pairs of consecutive surveys (e.g. Ledwell et al.'s 1998's estimates of second moments).

321 sinking in the SML, rapid upwelling in the BBL, and slow upwelling in between the two (Figure
 322 7a, stars). These promising results suggest that equation (10) offers a novel practical method for
 323 estimating buoyancy velocities from TREs based on Ruan and Ferrari (2021)'s tracer-weighted
 324 buoyancy moment equations, with the caveat that we have assumed perfect spatial information at
 325 instantaneous surveys at both t_0 and t_1 .

333 Watermass transformations provide a helpful reference for contextualizing the magnitude and
 334 vertical structure of tracer-weighted velocities. In Appendix B, we convert the height-above-bottom
 335 (or η) structure of watermass transformations into an effective vertical velocity versus η -profile
 336 (see Appendix B),

$$\overline{W}^T(\eta) \equiv \frac{\sin \theta}{L_y} \frac{\partial}{\partial \eta} \overline{\mathcal{E}}^T(\eta). \quad (11)$$

337 This metric reveals that vigorous upwelling of $O(4 \times 10^{-5} \text{ m/s})$ is on average confined to the 40m-
 338 thick BBL, largely compensated by downwelling an order of magnitude weaker and broader in the
 339 SML above (Figure 8b-d, grey lines). This would superficially seem to be inconsistent with the
 340 tracer diagnostics, which exhibit weaker BBL upwelling that extends an order of magnitude higher
 341 above the bottom.

342 The key to reconciling the two diagnostics is that the tracer distributions, while initially compact,
 343 rapidly spread in η -space (Figure 5c,g,k). To demonstrate the effect of this spreading on the tracer
 344 diagnostics, we convolve the vertical velocity versus η -profile (11) with smoothing tracer kernels
 345 of different shapes and widths (Figure 8a),

$$\overline{W}(\eta) \approx \int_{-\infty}^{\infty} \mathcal{K}(\eta - \eta') \overline{W}^T(\eta') d\eta'. \quad (12)$$

346 Tracer kernels with widths less than the thickness of the BBL accurately reproduce its η -structure,
 347 while thicker kernels begin smearing the BBL and SML together, reducing both of their magnitudes
 348 and elevating the apparent interface between them (Figure 8b,c,d). This smearing effect is partic-
 349 ularly dramatic for exponential kernels with thick tails, which reasonably approximates the shapes
 350 of the Crest and Bottom tracers for most of the experiment (Figure 5g,k). Indeed, convolving the
 351 vertical velocity η -profile with exponential kernels of the same approximate width of these tracers
 352 reasonably reproduces the tracer-diagnosed η -structure of the buoyancy velocity (Figure 8d). By
 353 contrast, the buoyancy velocity experienced by the BBTRE tracer is not as severely convoluted

354 (Figure 8b-d) because it neither spreads as rapidly nor does it feel much of the compensating BBL
 355 upwelling (Figure 5c).

356 *c. Bottom-enhanced diapycnal tracer spreading*

357 Over the course of the experiment, all three tracers spread across isopycnals on average. As
 358 anticipated from the prescribed bottom-enhanced diffusivity profile: the closer a tracer is released
 359 to the bottom, the faster it spreads (Figure 7a; stars). However, this time-mean view obscures
 360 surprisingly large temporal variability (Figure 6f,h). This tendency is particularly dramatic for
 361 the Bottom tracer, which experiences extremely rapid diapycnal spreading in the first 150 days
 362 but, by day 350, stops spreading entirely and even begins temporarily *contracting* in buoyancy
 363 space (Figure 6h)! The interpretation of diapycnal tracer spreading is more subtle than that of
 364 the mean diapycnal motion of the tracer, since two separate terms contribute to spreading: the
 365 tracer-weighted effective diffusivity κ_{Taylor} and diapycnal stretching κ_{ω} (eq. 4). The contribution
 366 from the tracer-weighted effective diffusivity is familiar from Taylor (1922)'s classic derivation,
 367 and is reasonably well approximated by the tracer-weighted in-situ diffusivity $\bar{\kappa}$ since correlations
 368 between the diffusivity and the squared temperature gradients are relatively small (Figure 6d,f,h),

$$\kappa_{\text{Taylor}} \equiv \frac{\overline{\kappa |\nabla T|^2}}{|\nabla T|^2} \approx \bar{\kappa}. \quad (13)$$

369 This contribution to diapycnal spreading from the tracer-weighted diffusivity remains roughly
 370 constant in time, aside from an initial transient as the tracer spreads towards shallower topographic
 371 features (Figures 7b). In contrast, the diapycnal stretching effect drives the substantial temporal
 372 variability in the diapycnal spreading experienced by the tracers (Figure 6d,f). Depending on the
 373 instantaneous distribution of the tracer, this term can vary substantially both in magnitude and sign,
 374 either amplifying the tracer-weighted diffusivity by up to 100% or off-setting it entirely (Figure
 375 7b,c; at 40 and 400 days, respectively).

376 *d. Disentangling diapycnal stretching and contraction effects*

377 Motivated by the bi-modal example in Section b, we decompose the diapycnal stretching term
 378 κ_{ω} by binning its contributions in (ω, T) space (Figure 9, as in Figure 1b), i.e. by decomposing the

379 volume integral into a sum over sub-volumes:

$$\frac{\kappa_{\omega}}{\kappa_{\text{Taylor}}} = \sum_{i,j} \int_{\mathcal{V}_{\{\omega_i\},\{T_j\}}} \frac{2\omega'T'c}{\mathcal{M}|\nabla T|^2 \kappa_{\text{Taylor}}} dV, \quad (14)$$

380 where $\mathcal{M} \equiv \int_{\mathcal{V}} c dV$ is the total tracer mass and the intersection of subsets $\{\omega_i\}$ and $\{T_j\}$ correspond
 381 to distinct sub-volumes $\mathcal{V}_{\{\omega_i\},\{T_j\}}$ of the tracer distribution, defined by their (ω, T) characteristics.
 382 Figure 9 shows heatmaps of the contributions from relatively narrow (ω', T') bins as well as the
 383 summed contributions from each of the quadrants delineated by the respective signs of ω' and T' .
 384 In (14) and throughout this section, we normalize by the total effective diapycnal diffusion κ_{Taylor}
 385 to quantify the relative importance of the unconventional stretching effects compared to the more
 386 conventional diapycnal diffusion; for example, $\kappa_{\omega}/\kappa_{\text{Taylor}} = 100\%$ implies stretching doubles the
 387 diffusive spreading rate while $\kappa_{\omega}/\kappa_{\text{Taylor}} = -100\%$ implies net stretching is sufficiently negative
 388 (i.e. contraction) to exactly offset the diffusive spreading.

389 We begin by exploring why the BBTR tracer experiences very little net diapycnal stretching,
 390 in contrast to the idealized SML simulation of Ruan and Ferrari (2021). At day 100 (Figure 9a),
 391 for example, the tracer is diapycnally stretched ($\overline{\omega'T'} > 0$) by an additional $23\% \kappa_{\text{Taylor}}$ (hereafter
 392 dropping the κ_{Taylor} for convenience) as relatively cold tracer relatively downwells ($T' < 0, \omega' < 0$)
 393 and relatively warm tracer relatively upwells ($T' > 0, \omega' > 0$). This stretching of 23% is so far
 394 consistent with Ruan and Ferrari (2021)'s idealized result of 18% additional stretching. However,
 395 a very small amount of cold tracer has made it close enough to the seafloor to be entrained in the
 396 BBL, where it upwells vigorously and results in a contraction effect of -9% which, supplemented
 397 by an additional -2% contraction from warm downwelling tracer, results in a reduction of the net
 398 diapycnal stretching to only $23\% - 11\% = 12\%$. By day 440, this patch of tracer is pulled further
 399 towards the bottom and its stretching effect grows to 69% , but is offset by an even larger diapycnal
 400 contraction of -76% in the BBL (Figure 9b); combined, these diapycnal stretching effects have
 401 a negligible effect of reducing diapycnal spreading by only -6% , in contrast to the continued
 402 strengthening of stretching effects⁵ predicted by Ruan and Ferrari (2021).

413 At the other extreme, we aim to understand how the Bottom tracer undergoes first a large net
 414 diapycnal stretching effect and then an even larger net diapycnal contraction effect. Over the

⁵Ruan and Ferrari (2021) acknowledge stretching may eventually be limited by boundary suppression (as in Holmes et al. 2019), but do not elaborate on its relative timing or magnitude.

415 first 100 days, most of the tracer upwells in the BBL and warms (Figure 6g). Some of the
416 warmest tracer remains in the BBL, where its upwelling drives a substantial diapycnal stretching
417 of 91% (Figure 9c). However, part of this warm branch of the tracer is entrained into the SML,
418 where its downwelling drives a largely compensating diapycnal contraction effect of -80% . The
419 relatively cold patch of tracer that is left behind contributes a stretching of $41\% - 15\% = 26\%$,
420 dominated by its relatively slow upwelling ($\omega > 0$ but $\omega' < 0$), bringing the net diapycnal stretching
421 to $91\% - 80\% + 26\% = 37\%$. By day 440, however, both modes of the tracer distribution (Figure
422 5l) drive large diapycnal contraction effects: -98% due to cold upwelling upstream of the sill and
423 -101% due to warm downwelling downstream of the sill (Figures 5j,l 9d). Diapycnal stretching
424 of 93% from the other quadrants offset about half of this diapycnal stretching effect, but the
425 net diapycnal contraction of -106% still overwhelms the spreading due to the in-situ diffusivity,
426 causing the Bottom tracer to temporarily contract in buoyancy space—countering conventional
427 intuition about the average effects of down-gradient diapycnal diffusion.

430 5. Discussion and Conclusion

431 By applying Ruan and Ferrari (2021)'s buoyancy-moment diagnostics to our quasi-realistic
432 regional simulation of mixing-driven abyssal flows (described in detail in a submitted companion
433 manuscript, Drake et al. 2022), we confirm the qualitative results of Holmes et al. (2019)'s
434 idealized analysis of the BBTRE release in the SML: over time, boundary suppression in the
435 BBL almost exactly compensates for vertical stretching in the SML, such that the net diapycnal
436 spreading of the BBTRE tracer coincidentally provides a reasonably accurate ($\pm 20\%$) estimate
437 of the tracer-weighted in-situ diffusivity (Figure 6d). These simulation results are supported by
438 a recent re-analysis of the BBTRE observations, which reveal a similarly negligible diapycnal
439 stretching effect of $< 5\% \kappa_{\text{Taylor}}$ (Figure 6d; Ledwell, personal communication). Quantitatively,
440 however, the diapycnal spreading we simulate for the BBTRE tracer is smaller than the observed
441 spreading by a factor of 2 (Figures 6d, 11), suggesting either the microstructure measurements
442 we use to tune the prescribed diffusivity profile are biased low or our simulation is missing other
443 unknown tracer dispersion processes. This is consistent with Ledwell (in prep)'s inversion of a
444 1D advection-diffusion model, which produced optimal diffusivities about twice as large as the
445 microstructure's sample-mean. Our results are also consistent with the conclusion of the submitted

446 companion manuscript (Drake et al. 2022), which shows that biases in the simulated flows and
447 stratification of the BBTRE fracture zone canyon also suggest the imposed microstructure mixing
448 rates may be biased low by a factor of roughly 2. These BBTRE-specific results are consistent
449 with the broader observational literature, which unanimously finds that mixing rates estimated
450 from TREs are larger than those suggested by co-located microstructure measurements (Ruan and
451 Ferrari 2021).

456 In contrast to the BBTRE release, we find that for near-bottom tracers diapycnal stretch-
457 ing/contraction effects can be of either sign (depending on the tracer distribution) and of com-
458 parable magnitude to the tracer-weighted in-situ diffusivity, $|\kappa_\omega| \sim \kappa_{\text{Taylor}} \simeq \bar{\kappa}$ (Figure 6h). Our
459 simulations demonstrate that three-dimensional eddies and topographic effects have a leading or-
460 der effect on diapycnal tracer spreading, as tracer distributions are chaotically transported in and
461 out of regions of vigorous mixing. Unsurprisingly, diapycnal stretching and contraction effects are
462 much stronger—and more variable—in our three dimensional flows over rough topography than
463 the already substantial effects reported by Holmes et al. (2019) for two-dimensional tracer trans-
464 port under one-dimensional boundary layer dynamics with parameterized isopycnal eddy stirring.
465 For our Bottom tracer release, for example, diapycnal stretching amplifies diapycnal spreading by
466 $O(100\% \kappa_{\text{Taylor}})$ in the first few dozen days of the simulation but suppresses diapycnal spreading
467 by $O(-100\% \kappa_{\text{Taylor}})$ for the last few dozen days (Figures 6h; 7c).

468 Given that rough topography generally implies strong bottom-enhanced diapycnal mixing (Polzin
469 et al. 1997; Waterhouse et al. 2014), which is in turn thought to incite bottom mixed layer eddies
470 (Callies 2018; Wenegrat et al. 2018; Ruan and Callies 2020), significant diapycnal stretching and
471 contraction effects are to be expected near sloping rough topography in the abyss, such as along
472 the global mid-ocean ridge system (Ledwell et al. 2000; Thurnherr et al. 2005, 2020) and within
473 continental slope canyons (Nazarian et al. 2021; Hamann et al. 2021; Albery et al. 2017). In these
474 regions, unlike for interior ocean releases such as BBTRE, tracer-based estimates of mixing rates
475 must take into account the three-dimensional history of the tracer distribution’s evolution.

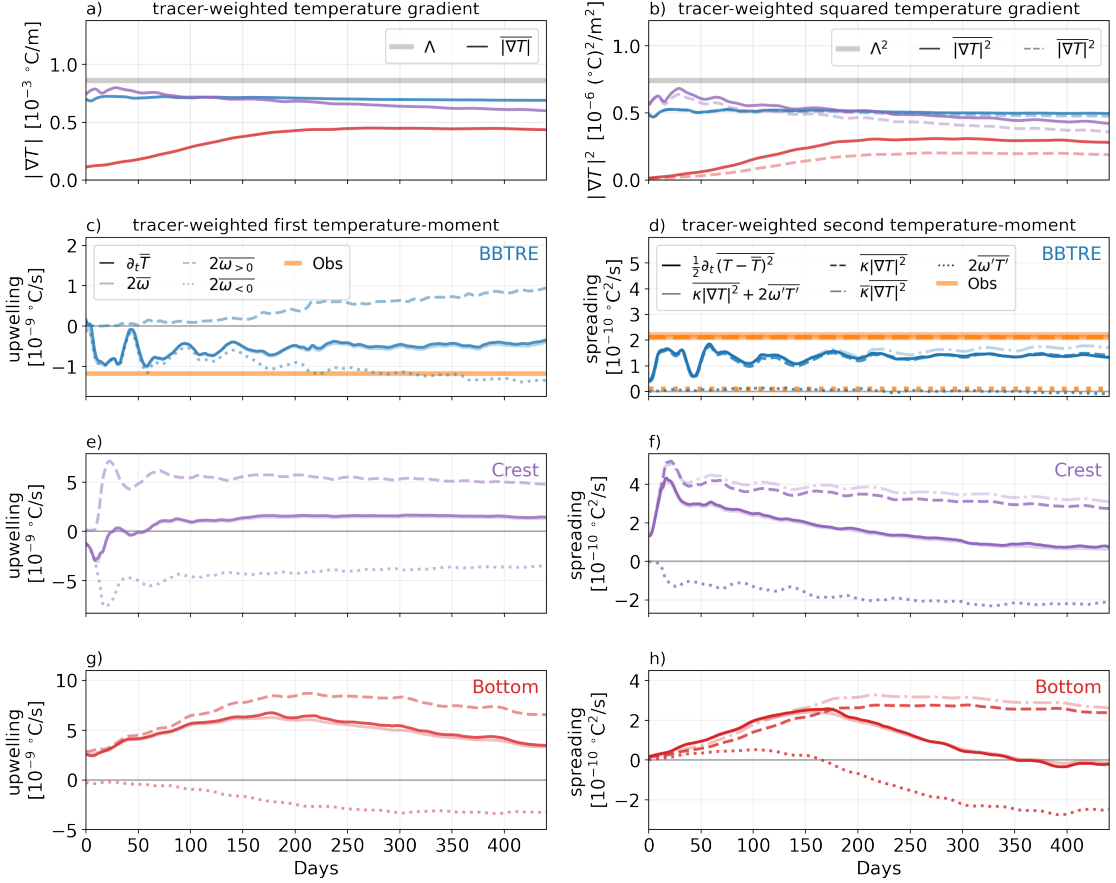
476 It has long been appreciated that the interpretation of tracer spreading near topography requires
477 greater care because of enhanced boundary mixing and hypsometric effects (e.g. Ledwell and
478 Hickey 1995). Attempts to modify the conventional 1D model to include these boundary effects
479 are varied: by separating the tracer distribution into "boundary" and "interior" regions (Ledwell and

480 Hickey 1995; Ledwell et al. 2016), by allowing vertical structure in the diffusivity profile (Ledwell
481 et al. 2000), or by extending the 1D model to a 2D (Watson et al. 2013) or 3D (Mackay et al.
482 2018) model to account for lateral transport into and out of regions of strong mixing. However,
483 the ad-hoc derivations of these models render them difficult to interpret and compare, suggesting
484 a complementary role for the more exact buoyancy-moment approach (Ruan and Ferrari 2021).

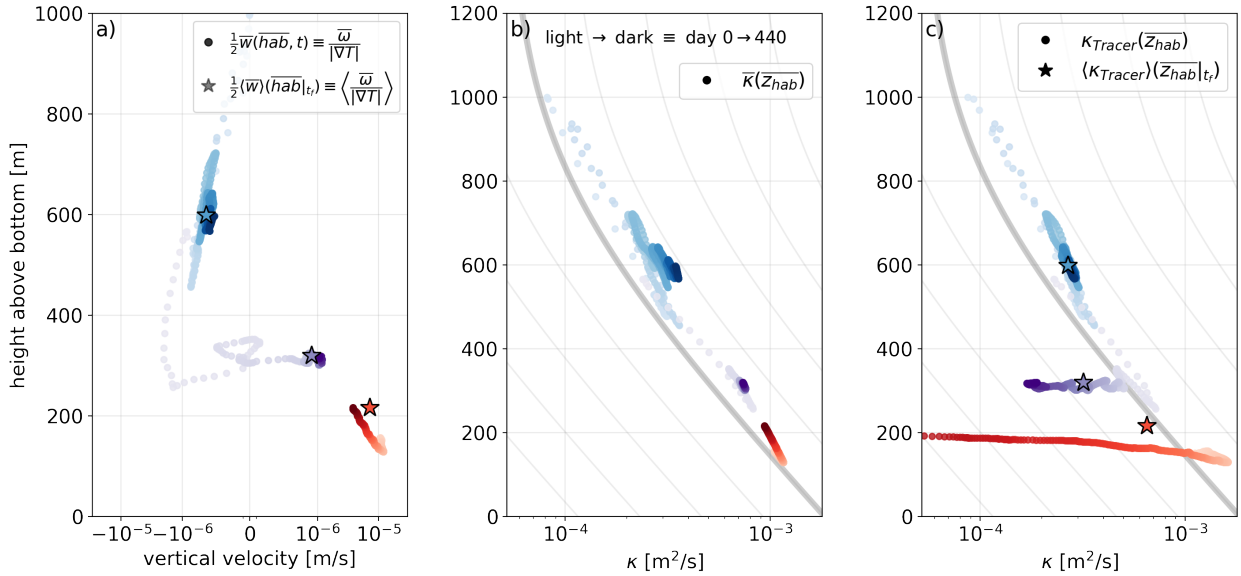
485 Mesoscale/submesoscale-resolving regional simulations of TREs are now feasible thanks to
486 exponential increases in computational power (Tulloch et al. 2014; Mashayek et al. 2017; Ogden et
487 al., in prep; this study) and have been used *a posteriori* to help interpret observations and explain
488 differences between mixing rates inferred from TREs and microstructure profiles. However, such
489 simulations have not yet been used to evaluate (or improve upon) operational methods for comparing
490 tracer and microstructure observations, such as by using a "perfect model" framework in which
491 simulated tracer observations are inverted in an attempt to recover the prescribed "true" diffusivity
492 field. Similarly, *a priori* or real-time numerical simulations could be used to inform future TRE
493 sampling strategies (current best practice is to roughly estimate horizontal transport from real-time
494 velocity estimates from ADCPs or altimetry; Messias and Ledwell, personal communication). To
495 our knowledge, this has not yet been done, with the notable exception of the *Bottom Boundary*
496 *Layer Turbulence and Abyssal Recipes* team (BLTTRE; NSF Award #1756251), who are using
497 TRE simulations to inform the experiment's planning and sampling strategies.

498 While our results suggest that estimates of in-situ diffusivity profiles from observations of a
499 tracer's *second* buoyancy moment may be corrupted by complicated diapycnal stretching processes
500 (Figure 7c; consistent with Holmes et al. 2019), they also suggest that the *first* buoyancy moment
501 provides a more robust and straight-forward estimate of the tracer-weighted in-situ turbulent buoy-
502 ancy flux convergence (or buoyancy velocity ω ; Figure 7a). However, if the width of the tracer
503 distribution is longer than the scale of flow variations, or if the tails are sufficiently thick, even the
504 first moment diagnostics can be a misleading combination of upwelling and downwelling flows
505 (Figure 8). Nevertheless, as long as a sizable fraction (here $\gg \overline{W}_{\text{SML}}^T / \overline{W}_{\text{BBL}}^T \approx 10\%$; Figure 8) of
506 the tracer remains in the BBL, the change in the first tracer-weighted buoyancy-moment is likely
507 to provide at least a reasonable lower-bound estimate of the average in-situ buoyancy velocity in
508 the BBL (Section 2b). This is a promising result in light of the ongoing BLTTRE, which aims to
509 provide the first in-situ estimates of BBL upwelling. Short-term surveys, when the tracer distribu-

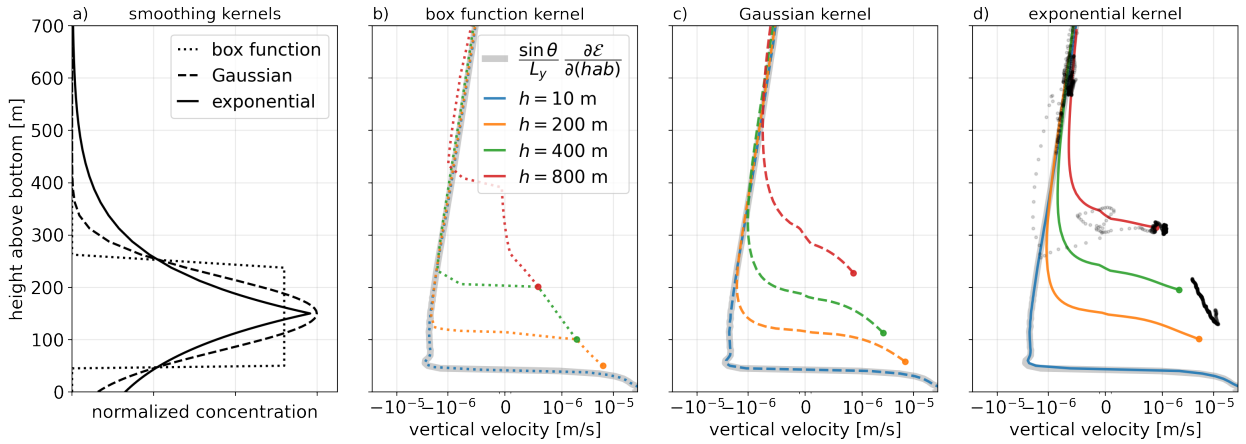
510 tion is still relatively compact (e.g. from a dye release experiment)—may be interpreted as lower
511 bound estimates of BBL upwelling—while long-term surveys—when the tracer roughly equally
512 occupies the BBL and SML—may be interpreted as estimates of net upwelling. Combined, these
513 two estimates could constrain the strength of the amplification factor, the ratio of strictly upwelling
514 transport in the BBL to net upwelling, which is predicted by theory to be much larger than 1 (Ferrari
515 et al. 2016; McDougall and Ferrari 2017; Callies 2018; Holmes and McDougall 2020). In com-
516 bination with previous observations of tracer-weighted diapycnal sinking in the SML above rough
517 topography (Ledwell et al. 2000), observations of vigorous tracer-weighted diapycnal upwelling in
518 the BBL would be compelling direct evidence for the emerging paradigm of bottom mixing layer
519 control of the abyssal meridional overturning circulation (Ferrari et al. 2016; de Lavergne et al.
520 2016a; Callies 2018; Callies and Ferrari 2018; Drake et al. 2020; submitted companion manuscript,
521 Drake et al. 2022).



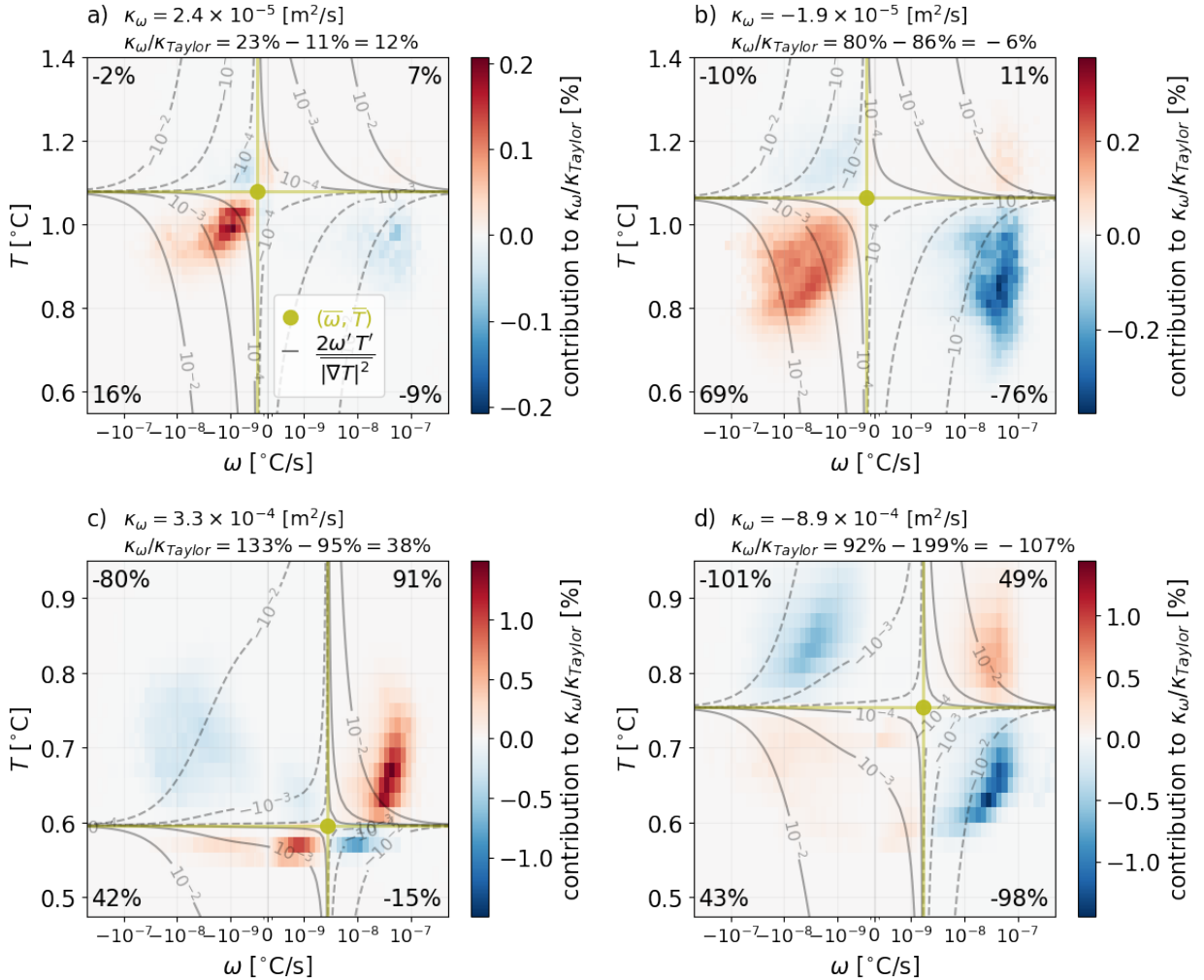
272 FIG. 6. Decomposition of the first and second tracer-weighted temperature moment tendencies, i.e. the rates
 273 of diapycnal motion and spreading, in terms of their driving mixing processes. The realistic BBTRE release is
 274 shown in blue, the Crest release in purple, and the Bottom release in red. (a-b) show the temporal evolution of the
 275 tracer-weighted stratification and stratification squared, with the background stratification $\Lambda \equiv \frac{dT_b}{dz}$ for reference
 276 (see Appendix A). (c-h) show the temporal evolution of the first and second moment tendencies (opaque solid
 277 lines) which are visually indistinguishable from the sum of the contributing mixing processes (transparent solid
 278 lines; demonstrating that spurious numerical mixing is negligible), as described by the left- and right-hand-sides
 279 of equations (3), $\partial_t \bar{T} = 2\bar{\omega}$, and (4), $\frac{1}{2} \partial_t \overline{(T - \bar{T})^2} = \overline{\kappa |\nabla T|^2} + 2\overline{\omega' T'}$, respectively. Orange lines in (c,d) show the
 280 time-averaged BBTRE moment tendencies estimated from observations, where the κ used in the right-hand-side
 281 terms is a height-above-bottom profile estimated from an inverse model (Ledwell et al. 1998, revised by Ledwell,
 282 in prep). (c,e,g) Dashed and dotted lines show the contributions from strictly upwelling and strictly downwelling
 283 regions, respectively. (d,f,h) Dashed lines show the contribution from tracer-weighted in-situ diffusion κ_{Taylor}
 284 (approximately equal to the tracer-weighted in-situ diffusivity $\bar{\kappa}$; dash-dotted lines) and dotted lines show the
 285 contribution from diapycnal stretching κ_{ω} .



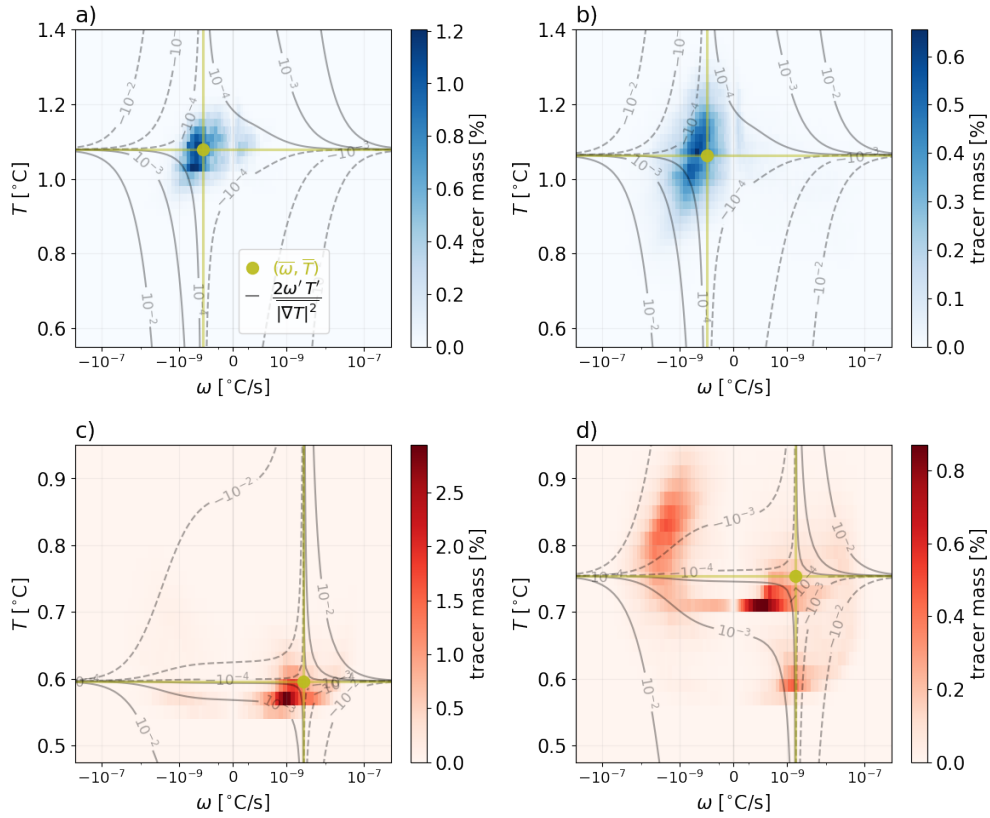
297 FIG. 7. (a) Height-above-bottom-averaged tracer-weighted buoyancy velocity, normalized by the buoyancy
 298 gradient to yield an effective vertical velocity (colors). (b,c) As in (a), but for the tracer-weighted in-situ
 299 diffusivity $\bar{\kappa}$ and tracer diffusivity κ_{Tracer} . Dots show trajectories (colors darkened over time) in terms of the
 300 magnitude of moment tendency terms and the tracer-weighted height-above-bottom $\overline{hab}(t)$. Stars in (a,c) show
 301 the time-averaged moments, as they would be estimated from a TRE survey 440 days after release (assuming
 302 perfect spatial coverage).



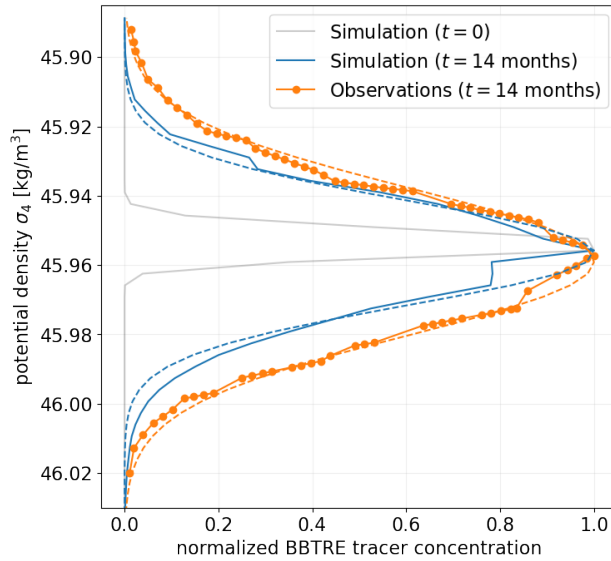
326 FIG. 8. Understanding the height-above-bottom structure of tracer transport by convolving the average velocity
 327 profile with idealized tracer kernels. (a) Three idealized shapes of tracer kernels, shown with a characteristic
 328 width of 200m meters and centered 150m above the bottom. (b-d) Grey lines show the height-above-bottom
 329 averaged effective vertical velocity, estimated using watermass transformation analysis (eq. 11). Colored lines
 330 show the result of convolving this profile with idealized kernels (eq. 12) of different shapes (columns) and widths
 331 (colors). Black dots in (d) reproduce the snapshots of tracer-weighted buoyancy velocities shown in Figure 7a,
 332 for comparison.



403 FIG. 9. Percentage contributions to the normalized net diapycnal stretching effect $\kappa_\omega/\kappa_{\text{Taylor}}$ from each (ω, T)
 404 bin, as a percentage, for the BBTRE (top) and Bottom (bottom) tracers at 100 days (left) and 440 days (right).
 405 The plotted quantity is the summand in eq. 14, which are integrated such that the contributions from each bin
 406 (log-spaced in ω) can be visually and quantitatively compared. Numbers in the four corners of each panel show
 407 the summed contributions from each of the four quadrants delineated by the respective signs of $\omega' \equiv \omega - \bar{\omega}$ and
 408 $T' \equiv T - \bar{T}$. The $\omega' = 0$ and $T' = 0$ lines in olive delineate the four quadrants. For reference, grey contours
 409 show the effective diapycnal stretching diffusivity, $\kappa_\omega \equiv 2\frac{\omega'T'}{|\nabla T|^2}$, that corresponds to each (ω, T) bin. Sub-
 410 titles decompose the net diapycnal stretching effect into strictly stretching ($\omega'T' > 0$) and strictly contracting
 411 components ($\omega'T' < 0$). PDFs of tracer mass show that a large portion of the tracers' mass does not contribute
 412 significantly to these stretching effects (Figure 10).



428 FIG. 10. Probability density function of tracer mass, as a percent contribution of each bin to the total tracer
 429 mass. Grey contours and olive lines as in Figure 9.



452 FIG. 11. Simulated and observed tracer distributions in density space at 14 months. We fit a Gaussian
 453 distribution $\propto \exp\left\{-\frac{(\sigma_4 - \sigma_{4,0})^2}{2\bar{\kappa}t}\right\}$ to the observations by eye (dashed orange). The simulated distribution is
 454 reasonably well fit by a Gaussian distribution corresponding to a diffusivity reduced by a factor of 2 (dashed
 455 blue), consistent with the results of the buoyancy moments method (Figure 6c,d).

522 *Acknowledgments.* We thank Jim Ledwell for countless insightful discussions about this work and
523 comments on previous versions of the manuscript. We acknowledge funding support from National
524 Science Foundation Awards 6932401 and 6936732. This material is based upon work supported by
525 the National Science Foundation Graduate Research Fellowship Program under Grant No. 174530.
526 Any opinions, findings, and conclusions or recommendations expressed in this material are those
527 of the author(s) and do not necessarily reflect the views of the National Science Foundation.

528 *Data availability statement.* The source code for the MITgcm simulations and all of the Python
529 code necessary to produce the figures will be publicly available at [github.com/hdrake/](https://github.com/hdrake/sim-bbtre)
530 `sim-bbtre` upon acceptance (or earlier by requesting the corresponding author). Our analysis
531 of labeled data arrays is greatly simplified by the `xarray` package in Python (Hoyer and Hamman
532 2017).

533 APPENDIX A

534 **A slope-native MITgcm configuration of mixing layer flows in the Brazil Basin**

535 We use a hydrostatic formulation of the MIT General Circulation Model (MITgcm; Marshall
536 et al. 1997) to simulate mixing-driven flows in the BBTRE canyon and the transient evolution of
537 three localized tracer releases. Regional bathymetry is extracted from the Global Bathymetry and
538 Topography at 15 Arc Sec dataset (SRTM15+; Tozer et al. 2019) and interpolated onto a locally-
539 tangent Cartesian grid $(\hat{x}, \hat{y}, \hat{z})$ aligned with the BBTRE canyon, where \hat{x} denotes the along-canyon
540 (or cross-ridge) dimension, \hat{y} denotes the cross-canyon (or along-ridge) dimension, and $\hat{d}(\hat{x}, \hat{y})$ is
541 the seafloor depth (Figure 2a). The domain includes both the BBTRE tracer release location and
542 ample room for up-canyon advection of the tracer, which is anticipated based on both the BBTRE
543 observations (Ledwell et al. 2000) and bottom boundary layer theory (Holmes et al. 2019).

544 Inspired by 1D boundary layer theory and the idealized 3D simulations of Callies (2018), we
545 configure a slope-native implementation of the MITgcm (only summarized here; details in Drake
546 et al., in prep). First, we separate a quiescent ($\mathbf{u}_b \equiv \mathbf{0}$) background with uniform stratification
547 $\Lambda \equiv \frac{dT_b}{d\hat{z}} = 9 \times 10^{-4} \text{ }^\circ\text{C/m}$ from the solution and solve only for the perturbations $T_p \equiv T - T_b$ and
548 $\mathbf{u}_p \equiv \mathbf{u} - \mathbf{u}_b$ about this background state, which requires adding the appropriate tendency terms to
549 the perturbation temperature and momentum equations, respectively. Second, we transform the
550 MITgcm into the coordinates of the mean slope, with slope angle $\theta = 1.26 \times 10^{-3}$ (Figure 2b),

551 allowing us to apply periodic boundary conditions to the perturbations in the (x, y) plane of the
552 mean slope. The de-trended seafloor depth is given by $d(x, y) \equiv \hat{d}(\hat{x}, \hat{y}) - \hat{x} \tan \theta$. Mean cross-
553 slope upwelling and downwelling across the periodic \mathbf{x} boundary provide infinite sources of dense
554 and light waters, respectively, allowing equilibration of the solution without requiring an explicit
555 restoring force to balance the homogenizing tendency of turbulent mixing (Garrett 1991).

556 A submitted companion paper (Drake et al. 2022) explores the mixing-driven circulations that
557 arise in this simulation in detail. Bottom-enhanced mixing spins up a broad diapycnal sinking
558 in the well-stratified interior and a vigorous diabatic upwelling in the bottom boundary layer.
559 Despite a modest restratifying effect by this mean overturning circulation, the solution develops a
560 substantial horizontal temperature gradient which stores available potential energy. This available
561 potential energy fuels instabilities, which grow to finite amplitude and are characterized by a
562 Rossby number of $R_o \approx 1$, i.e. are submesoscale in nature (see e.g. McWilliams 2016). One
563 effect of these eddies is to restratify the bottom 20m or so, bringing the simulated stratification
564 more in line with observations than 1D boundary layer dynamics would suggest (Callies 2018;
565 Ruan and Callies 2020). A hierarchy of progressively simplified versions of the simulation are
566 used as mechanism denial experiments to show the importance of different dynamical processes
567 in controlling the near-bottom stratification, which in turn controls the magnitude of near-bottom
568 diapycnal upwelling.

569 In our slope-native configuration, one should imagine infinitely many copies of TREs, each
570 separated by a horizontal distance $L_x = 480\text{km}$ (domain length) and vertical height $L_x \tan \theta \approx$
571 1000m (corresponding to a background temperature difference $\Delta T \approx \frac{dT_b}{dz} L_x \sin \theta = 0.52^\circ\text{C}$). A
572 limitation of this configuration is that by 1000 days enough of the tracer crosses the periodic
573 boundaries that the copies of the tracers begin significantly interfering with each other and the
574 temperature moment calculations become meaningless, which is why we truncate the simulations
575 after the timing of the first BBTRE survey (14 months ≈ 440 days). For all of the analysis presented
576 here, we re-center our periodic domain on the center of mass of a single copy of the tracer cloud
577 before adding the background state (i.e. the constantly stratified background temperature field T_b)
578 back in and then we crop the infinite domain to ignore other copies of the tracer (similar to the
579 approach used to compute watermass transformations in Appendix B).

Eulerian and tracer-weighted watermass transformations

A natural framework for understanding the drivers of diapycnal transport is watermass transformation analysis (Walin 1982; Marshall et al. 1999), which reframes the buoyancy budget in buoyancy space by integrating along buoyancy surfaces (or over buoyancy classes). Following Ferrari et al. (2016), the diapycnal transport $\mathcal{E}(T, t)$ across a buoyancy surface $\mathcal{A}(T)$ is given by

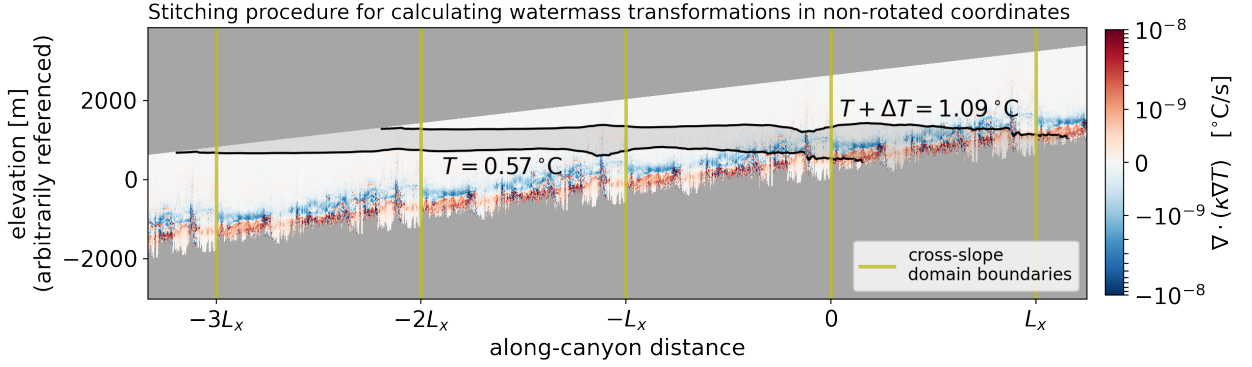
$$\mathcal{E}(T, t) \equiv \iint_{\mathcal{A}(T)} \mathbf{e} \cdot \mathbf{n} \, dA = \partial_T \int_{\mathcal{V}(\tilde{T} < T)} \omega \, dV, \quad (\text{B1})$$

where $\mathbf{e} \equiv \left(\mathbf{u} \cdot \mathbf{n} - \frac{T_t}{|\nabla T|} \right) \mathbf{n}$ is the diapycnal velocity and $\mathcal{V}(\tilde{T} < T)$ is the volume enclosing any water denser than T . Since our simulations have not fully equilibrated in the SML, diapycnal transports include two components: flow across a buoyancy surface and the movement of the buoyancy surfaces themselves. In the present context, it is useful to distinguish contributions to the diapycnal transport from a strictly upwelling BBL component, where the integral is only evaluated over the strictly upwelling volume $\mathcal{V}(\tilde{T} < T; \omega > 0)$, and a strictly downwelling SML component, similarly defined (see Figure B1).

In practice, meaningful evaluation of this integral in the slope-native configuration requires stitching together $H/(L_x \tan \theta) \approx O(5)$ periodic copies of the domain (where H is the height of the domain) before adding in the background buoyancy field B , so that each isopycnal can be followed all the way from its incrop at the seafloor to the interior far-field where mixing is weak (Figure B1). Further, because our simulation is periodic in the cross-slope direction (and thus in mean buoyancy), the resulting watermass transformations are periodic over a buoyancy interval $\Delta T = \Lambda L_x \tan \theta \approx 0.52^\circ\text{C}$. Temporal variability of watermass transformations is small relative to the other variations we focus on, so all results hereafter refer to their time-mean.

Averaging over a buoyancy layer of thickness ΔT yields a single representative value of the net watermass transformation,

$$\bar{\mathcal{E}}^T \equiv \frac{1}{\Delta T} \int_T^{T+\Delta T} \mathcal{E}(\tilde{T}) \, d\tilde{T} = \int_{\mathcal{V}(T < \tilde{T} < T+\Delta T)} \frac{\omega}{\Delta T} \, dV. \quad (\text{B2})$$



601 FIG. B1. Turbulent buoyancy (temperature) flux convergence along the trough of the BBTRE canyon. Vertical
 602 olive lines show along-canyon boundaries of the simulation domain; the solution is doubly periodic in buoyancy
 603 perturbations, but discontinuous in the total buoyancy in the along-canyon direction due to a constant background
 604 mean slope and stratification. For the small mean slopes considered here, computing watermass transformations
 605 thus requires reconstructing the full extent of buoyancy surfaces by stitching together multiple copies of the
 606 domain, each translated by a multiple of the domain extent L_x and by a background temperature jump $\Delta T =$
 607 $\Lambda \Delta z \approx 0.52^\circ\text{C}$ (where $\Delta z = L_x \tan \theta$ is the layer thickness).

610 This equation is also reminiscent of that for the evolution of the first tracer-weighted buoyancy
 611 moment (3), with the whole domain being weighted equally as opposed to being weighted by the
 612 tracer concentration.

613 The detailed height-above-bottom (η , for short) structure of upwelling and downwelling water-
 614 mass transformations are also of interest, since these are more directly comparable with measure-
 615 ments from vertical profilers, 1D BBL theory, and the diapycnal transport of localized tracers.
 616 Building upon Holmes and McDougall (2020), we define the height-above-bottom cumulative
 617 watermass transformation as:

$$\overline{\mathcal{E}}^T(\eta) = \int_{\mathcal{V}(T_0 < \bar{T} < T_0 + \Delta T; \bar{\eta} < \eta)} \frac{\omega}{\Delta T} dV. \quad (\text{B3})$$

618 We aim to convert these watermass transformations into effective vertical velocities, for more
 619 direct comparison with the tracer diagnostics. Loosely, taking the slope-normal (or η) derivative

620 provides the up-slope upwelling flux (in m^2/s) at a given height-above-bottom:

$$\frac{\partial \overline{\mathcal{E}}^T(\eta)}{\partial \eta} = \frac{\partial}{\partial \eta} \int_{\mathcal{V}(T_0 < \tilde{T} < T_0 + \Delta T; \tilde{\eta} < \eta)} \frac{\omega}{\Delta T} dV. \quad (\text{B4})$$

621 Multiplying by $\sin \theta$ approximately converts this to a vertical flux, and dividing by the width L_y
622 of the domain finishes the conversion to the effective velocity (11). Profiles of $\overline{W}^T(\eta)$ are shown in
623 Figure 8 and, after convolution with idealized height-above-bottom tracer distributions, compare
624 favorably with the diagnosed vertical structure of tracer upwelling.

625 References

626 Abernathey, R. P., I. Cerovecki, P. R. Holland, E. Newsom, M. Mazloff, and L. D. Talley, 2016:
627 Water-mass transformation by sea ice in the upper branch of the Southern Ocean overturning.
628 *Nature Geoscience*, **9** (8), 596–601, <https://doi.org/10.1038/ngeo2749>, URL <http://www.nature.com/articles/ngeo2749>, publisher: Nature Publishing Group.

630 Albery, M. S., S. Billheimer, M. M. Hamann, C. Y. Ou, V. Tamsitt, A. J. Lucas, and
631 M. H. Alford, 2017: A reflecting, steepening, and breaking internal tide in a submarine
632 canyon. *Journal of Geophysical Research: Oceans*, **122** (8), 6872–6882, <https://doi.org/10.1002/2016JC012583>, URL <https://onlinelibrary.wiley.com/doi/abs/10.1002/2016JC012583>,
633 [_eprint: https://onlinelibrary.wiley.com/doi/pdf/10.1002/2016JC012583](https://onlinelibrary.wiley.com/doi/pdf/10.1002/2016JC012583).

636 Baker, M. A., and C. H. Gibson, 1987: Sampling Turbulence in the Stratified Ocean:
637 Statistical Consequences of Strong Intermittency. *Journal of Physical Oceanography*,
638 **17** (10), 1817–1836, [https://doi.org/10.1175/1520-0485\(1987\)017<1817:STITSO>2.0.CO;](https://doi.org/10.1175/1520-0485(1987)017<1817:STITSO>2.0.CO;2)
639 [2](https://journals.ametsoc.org/view/journals/phoc/17/10/1520-0485_1987_017_1817_stitso_2_0_co_2.xml), URL [https://journals.ametsoc.org/view/journals/phoc/17/10/1520-0485_1987_017_1817_](https://journals.ametsoc.org/view/journals/phoc/17/10/1520-0485_1987_017_1817_stitso_2_0_co_2.xml)
640 [_stitso_2_0_co_2.xml](https://journals.ametsoc.org/view/journals/phoc/17/10/1520-0485_1987_017_1817_stitso_2_0_co_2.xml), publisher: American Meteorological Society Section: Journal of Physical
640 Oceanography.

641 Bryan, K., and L. J. Lewis, 1979: A water mass model of the world ocean. *Journal of Geophysical*
642 *Research*, **84** (C5), 2503–2517, <https://doi.org/10.1029/JC084iC05p02503>, ISBN: 0148-0227.

643 Cael, B., and A. Mashayek, 2021: Log-Skew-Normality of Ocean Turbulence. *Physical Review*
644 *Letters*, **126** (22), 224 502, <https://doi.org/10.1103/PhysRevLett.126.224502>, URL <https://link>.

645 aps.org/doi/10.1103/PhysRevLett.126.224502, publisher: American Physical Society.

646 Callies, J., 2018: Restratification of Abyssal Mixing Layers by Submesoscale Baroclinic
647 Eddies. *Journal of Physical Oceanography*, JPO-D-18-0082.1, [https://doi.org/10.1175/
648 JPO-D-18-0082.1](https://doi.org/10.1175/JPO-D-18-0082.1), URL <http://journals.ametsoc.org/doi/10.1175/JPO-D-18-0082.1>.

649 Callies, J., and R. Ferrari, 2018: Dynamics of an Abyssal Circulation Driven by Bottom-Intensified
650 Mixing on Slopes. *Journal of Physical Oceanography*, **48** (6), 1257–1282, [https://doi.org/
651 10.1175/JPO-D-17-0125.1](https://doi.org/10.1175/JPO-D-17-0125.1), URL <http://journals.ametsoc.org/doi/10.1175/JPO-D-17-0125.1>.

652 Clément, L., A. M. Thurnherr, and L. C. St. Laurent, 2017: Turbulent Mixing in a Deep
653 Fracture Zone on the Mid-Atlantic Ridge. *Journal of Physical Oceanography*, **47** (8), 1873–
654 1896, <https://doi.org/10.1175/JPO-D-16-0264.1>, URL [http://journals.ametsoc.org/doi/10.1175/
656 JPO-D-16-0264.1](http://journals.ametsoc.org/doi/10.1175/
655 JPO-D-16-0264.1).

656 de Lavergne, C., G. Madec, J. Le Sommer, A. J. G. Nurser, and A. C. Naveira Garabato,
657 2016a: The Impact of a Variable Mixing Efficiency on the Abyssal Overturning. *Journal
658 of Physical Oceanography*, **46** (2), 663–681, <https://doi.org/10.1175/JPO-D-14-0259.1>, URL
659 <http://journals.ametsoc.org/doi/10.1175/JPO-D-14-0259.1>.

660 de Lavergne, C., G. Madec, J. Le Sommer, A. J. G. Nurser, and A. C. Naveira Garabato,
661 2016b: On the Consumption of Antarctic Bottom Water in the Abyssal Ocean. *Journal
662 of Physical Oceanography*, **46** (2), 635–661, <https://doi.org/10.1175/JPO-D-14-0201.1>, URL
663 <http://journals.ametsoc.org/doi/10.1175/JPO-D-14-0201.1>.

664 de Lavergne, C., and Coauthors, 2020: A Parameterization of Local and Re-
665 mote Tidal Mixing. *Journal of Advances in Modeling Earth Systems*, **12** (5),
666 e2020MS002065, <https://doi.org/https://doi.org/10.1029/2020MS002065>, URL
667 <https://agupubs.onlinelibrary.wiley.com/doi/abs/10.1029/2020MS002065>,
668 [_eprint:
https://agupubs.onlinelibrary.wiley.com/doi/pdf/10.1029/2020MS002065](https://agupubs.onlinelibrary.wiley.com/doi/pdf/10.1029/2020MS002065).

669 Dillon, T. M., 1982: Vertical overturns: A comparison of Thorpe and Ozmi-
670 dov length scales. *Journal of Geophysical Research: Oceans*, **87** (C12),
671 9601–9613, <https://doi.org/https://doi.org/10.1029/JC087iC12p09601>, URL <https://doi.org/https://doi.org/10.1029/JC087iC12p09601>.

672 //agupubs.onlinelibrary.wiley.com/doi/abs/10.1029/JC087iC12p09601, _eprint:
673 https://agupubs.onlinelibrary.wiley.com/doi/pdf/10.1029/JC087iC12p09601.

674 Drake, H. F., R. Ferrari, and J. Callies, 2020: Abyssal Circulation Driven
675 by Near-Boundary Mixing: Water Mass Transformations and Interior Stratifi-
676 cation. *Journal of Physical Oceanography*, **50** (8), 2203–2226, [https://doi.org/](https://doi.org/10.1175/JPO-D-19-0313.1)
677 10.1175/JPO-D-19-0313.1, URL [https://journals.ametsoc.org/jpo/article/50/8/2203/348530/](https://journals.ametsoc.org/jpo/article/50/8/2203/348530/Abyssal-Circulation-Driven-by-Near-Boundary-Mixing)
678 Abyssal-Circulation-Driven-by-Near-Boundary-Mixing, publisher: American Meteorological
679 Society.

680 Drake, H. F., X. Ruan, R. Ferrari, A. M. Thurnherr, K. Ogden, and J. Callies, 2022: Dynamics
681 of eddying abyssal mixing layers over rough topography. URL [https://eartharxiv.org/repository/](https://eartharxiv.org/repository/view/3000/)
682 view/3000/, publisher: EarthArXiv.

683 Ferrari, R., A. Mashayek, T. J. McDougall, M. Nikurashin, and J.-M. Campin, 2016: Turning Ocean
684 Mixing Upside Down. *Journal of Physical Oceanography*, **46** (7), 2239–2261, [https://doi.org/](https://doi.org/10.1175/JPO-D-15-0244.1)
685 10.1175/JPO-D-15-0244.1, URL <http://journals.ametsoc.org/doi/10.1175/JPO-D-15-0244.1>.

686 Garrett, C., 1991: Marginal mixing theories. *Atmosphere-Ocean*, **29** (2), 313–339,
687 <https://doi.org/10.1080/07055900.1991.9649407>, URL [http://www.tandfonline.com/doi/abs/10.](http://www.tandfonline.com/doi/abs/10.1080/07055900.1991.9649407)
688 1080/07055900.1991.9649407.

689 Garrett, C., P. MacCready, and P. Rhines, 1993: Boundary Mixing and Arrested Ekman Lay-
690 ers: Rotating Stratified Flow Near a Sloping Boundary. *Annual Review of Fluid Mechan-*
691 *ics*, **25** (1), 291–323, <https://doi.org/10.1146/annurev.fl.25.010193.001451>, URL [http://www.](http://www.annualreviews.org/doi/10.1146/annurev.fl.25.010193.001451)
692 [annualreviews.org/doi/10.1146/annurev.fl.25.010193.001451](http://www.annualreviews.org/doi/10.1146/annurev.fl.25.010193.001451), publisher: Annual Reviews 4139
693 El Camino Way, P.O. Box 10139, Palo Alto, CA 94303-0139, USA.

694 Garrett, C., and W. Munk, 1972: Space-Time scales of internal waves. *Geo-*
695 *physical Fluid Dynamics*, **3** (3), 225–264, <https://doi.org/10.1080/03091927208236082>,
696 URL <https://doi.org/10.1080/03091927208236082>, publisher: Taylor & Francis _eprint:
697 <https://doi.org/10.1080/03091927208236082>.

698 Garrett, C., and W. Munk, 1975: Space-time scales of internal waves:
699 A progress report. *Journal of Geophysical Research (1896-1977)*,

700 **80** (3), 291–297, <https://doi.org/10.1029/JC080i003p00291>, URL <https://agupubs.onlinelibrary.wiley.com/doi/abs/10.1029/JC080i003p00291>,
701 [_eprint:
702 https://agupubs.onlinelibrary.wiley.com/doi/pdf/10.1029/JC080i003p00291](https://agupubs.onlinelibrary.wiley.com/doi/pdf/10.1029/JC080i003p00291).

703 Gregg, M., E. D’Asaro, J. Riley, and E. Kunze, 2018: Mixing Efficiency in
704 the Ocean. *Annual Review of Marine Science*, **10** (1), 443–473, [https://doi.org/
705 10.1146/annurev-marine-121916-063643](https://doi.org/10.1146/annurev-marine-121916-063643), URL [http://www.annualreviews.org/doi/10.1146/
706 annurev-marine-121916-063643](http://www.annualreviews.org/doi/10.1146/annurev-marine-121916-063643).

707 Gregg, M. C., 1989: Scaling turbulent dissipation in the thermocline. *Journal of Geophysical
708 Research*, **94** (C7), 9686, <https://doi.org/10.1029/JC094iC07p09686>, URL [http://doi.wiley.com/
709 10.1029/JC094iC07p09686](http://doi.wiley.com/10.1029/JC094iC07p09686).

710 Gregg, M. C., T. B. Sanford, and D. P. Winkel, 2003: Reduced mixing from the breaking of internal
711 waves in equatorial waters. *Nature*, **422** (6931), 513–515, <https://doi.org/10.1038/nature01507>,
712 URL <https://www.nature.com/articles/nature01507>, number: 6931 Publisher: Nature Publishing
713 Group.

714 Hamann, M. M., M. H. Alford, A. J. Lucas, A. F. Waterhouse, and G. Voet, 2021: Tur-
715 bulence Driven by Reflected Internal Tides in a Supercritical Submarine Canyon. *Journal
716 of Physical Oceanography*, **51** (2), 591–609, <https://doi.org/10.1175/JPO-D-20-0123.1>, URL
717 <https://journals.ametsoc.org/view/journals/phoc/51/2/jpo-d-20-0123.1.xml>, publisher: Ameri-
718 can Meteorological Society Section: Journal of Physical Oceanography.

719 Henyey, F. S., J. Wright, and S. M. Flatté, 1986: Energy and action flow
720 through the internal wave field: An eikonal approach. *Journal of Geophysical
721 Research: Oceans*, **91** (C7), 8487–8495, <https://doi.org/10.1029/JC091iC07p08487>,
722 URL <https://agupubs.onlinelibrary.wiley.com/doi/abs/10.1029/JC091iC07p08487>,
723 [_eprint:
https://agupubs.onlinelibrary.wiley.com/doi/pdf/10.1029/JC091iC07p08487](https://agupubs.onlinelibrary.wiley.com/doi/pdf/10.1029/JC091iC07p08487).

724 Hogg, N., P. Biscaye, W. Gardner, and W. Jr, 1982: On the Transport and Modification of Antarctic
725 Bottom Water in the Vema Channel. *J. Mar. Res.*, **40**, 231–263.

726 Holmes, R. M., C. de Lavergne, and T. J. McDougall, 2019: Tracer Transport within Abyssal
727 Mixing Layers. *Journal of Physical Oceanography*, **49** (10), 2669–2695, <https://doi.org/10.1175/JPO-D-19-0123.1>

728 1175/JPO-D-19-0006.1, URL <https://journals.ametsoc.org/doi/full/10.1175/JPO-D-19-0006.1>,
729 publisher: American Meteorological Society.

730 Holmes, R. M., and T. J. McDougall, 2020: Diapycnal Transport near a Sloping Bottom
731 Boundary. *Journal of Physical Oceanography*, **50** (11), 3253–3266, [https://doi.org/10.1175/
732 JPO-D-20-0066.1](https://doi.org/10.1175/JPO-D-20-0066.1), URL [https://journals.ametsoc.org/view/journals/phoc/50/11/jpoD200066.
733 xml](https://journals.ametsoc.org/view/journals/phoc/50/11/jpoD200066.xml), publisher: American Meteorological Society Section: Journal of Physical Oceanogra-
734 phy.

735 Holtermann, P. L., L. Umlauf, T. Tanhua, O. Schmale, G. Rehder, and J. J.
736 Waniek, 2012: The Baltic Sea Tracer Release Experiment: 1. Mixing rates.
737 *Journal of Geophysical Research: Oceans*, **117** (C1), [https://doi.org/10.1029/
738 2011JC007439](https://doi.org/10.1029/2011JC007439), URL <https://onlinelibrary.wiley.com/doi/abs/10.1029/2011JC007439>, _eprint:
739 <https://onlinelibrary.wiley.com/doi/pdf/10.1029/2011JC007439>.

740 Hoyer, S., and J. Hamman, 2017: xarray: N-D labeled arrays and datasets in Python. *Journal of*
741 *Open Research Software*, **5** (1), <https://doi.org/10.5334/jors.148>, URL [http://doi.org/10.5334/
742 jors.148](http://doi.org/10.5334/jors.148).

743 Huang, R. X., and X. Jin, 2002: Deep Circulation in the South Atlantic Induced by Bottom-
744 Intensified Mixing over the Midocean Ridge*. *Journal of Physical Oceanography*, **32** (4),
745 1150–1164, [https://doi.org/10.1175/1520-0485\(2002\)032<1150:DCITSA>2.0.CO;2](https://doi.org/10.1175/1520-0485(2002)032<1150:DCITSA>2.0.CO;2).

746 Kunze, E., E. Firing, J. M. Hummon, T. K. Chereskin, and A. M. Thurnherr, 2006: Global
747 Abyssal Mixing Inferred from Lowered ADCP Shear and CTD Strain Profiles. *Journal of*
748 *Physical Oceanography*, **36** (8), 1553–1576, <https://doi.org/10.1175/JPO2926.1>, URL [https://
749 //journals.ametsoc.org/view/journals/phoc/36/8/jpo2926.1.xml](https://journals.ametsoc.org/view/journals/phoc/36/8/jpo2926.1.xml), publisher: American Meteorolo-
750 gical Society Section: Journal of Physical Oceanography.

751 Ledwell, J. R., T. F. Duda, M. A. Sundermeyer, and H. E. Seim, 2004: Mix-
752 ing in a coastal environment: 1. A view from dye dispersion. *Journal of*
753 *Geophysical Research: Oceans*, **109** (C10), [https://doi.org/https://doi.org/10.1029/
754 2003JC002194](https://doi.org/10.1029/2003JC002194), URL <https://agupubs.onlinelibrary.wiley.com/doi/abs/10.1029/2003JC002194>,
755 _eprint: <https://agupubs.onlinelibrary.wiley.com/doi/pdf/10.1029/2003JC002194>.

- 756 Ledwell, J. R., R. He, Z. Xue, S. F. DiMarco, L. J. Spencer, and P. Chap-
757 man, 2016: Dispersion of a tracer in the deep Gulf of Mexico. *Journal of Geo-*
758 *physical Research: Oceans*, **121** (2), 1110–1132, [https://doi.org/https://doi.org/10.1002/](https://doi.org/https://doi.org/10.1002/2015JC011405)
759 [2015JC011405](https://doi.org/https://doi.org/10.1002/2015JC011405), URL <https://agupubs.onlinelibrary.wiley.com/doi/abs/10.1002/2015JC011405>,
760 [_eprint: https://agupubs.onlinelibrary.wiley.com/doi/pdf/10.1002/2015JC011405](https://agupubs.onlinelibrary.wiley.com/doi/pdf/10.1002/2015JC011405).
- 761 Ledwell, J. R., and B. M. Hickey, 1995: Evidence for enhanced boundary mix-
762 ing in the Santa Monica Basin. *Journal of Geophysical Research: Oceans*,
763 **100** (C10), 20 665–20 679, <https://doi.org/https://doi.org/10.1029/94JC01182>,
764 URL <https://agupubs.onlinelibrary.wiley.com/doi/abs/10.1029/94JC01182>, [_eprint:](https://agupubs.onlinelibrary.wiley.com/doi/pdf/10.1029/94JC01182)
765 <https://agupubs.onlinelibrary.wiley.com/doi/pdf/10.1029/94JC01182>.
- 766 Ledwell, J. R., E. T. Montgomery, K. L. Polzin, L. C. St. Laurent, R. W. Schmitt, and J. M.
767 Toole, 2000: Evidence for enhanced mixing over rough topography in the abyssal ocean. *Nature*,
768 **403** (6766), 179–182, <https://doi.org/10.1038/35003164>, URL [http://www.nature.com/articles/](http://www.nature.com/articles/35003164)
769 [35003164](http://www.nature.com/articles/35003164), publisher: Nature Publishing Group.
- 770 Ledwell, J. R., A. J. Watson, and C. S. Law, 1998: Mixing of a tracer in the pycnocline. *Journal of*
771 *Geophysical Research: Oceans*, **103** (C10), 21 499–21 529, [https://doi.org/https://doi.org/10.](https://doi.org/https://doi.org/10.1029/98JC01738)
772 [1029/98JC01738](https://doi.org/https://doi.org/10.1029/98JC01738), URL <https://agupubs.onlinelibrary.wiley.com/doi/abs/10.1029/98JC01738>,
773 [_eprint: https://agupubs.onlinelibrary.wiley.com/doi/pdf/10.1029/98JC01738](https://agupubs.onlinelibrary.wiley.com/doi/pdf/10.1029/98JC01738).
- 774 Lele, R., and Coauthors, 2021: Abyssal Heat Budget in the Southwest Pacific Basin. *Journal*
775 *of Physical Oceanography*, **51** (11), 3317–3333, <https://doi.org/10.1175/JPO-D-21-0045.1>,
776 URL <https://journals.ametsoc.org/view/journals/phoc/51/11/JPO-D-21-0045.1.xml>, publisher:
777 American Meteorological Society Section: Journal of Physical Oceanography.
- 778 Lumpkin, R., and K. Speer, 2007: Global Ocean Meridional Overturning. *Journal of Physical*
779 *Oceanography*, **37** (10), 2550–2562, <https://doi.org/10.1175/JPO3130.1>, URL [http://dx.doi.org/](http://dx.doi.org/10.1175/JPO3130.1)
780 [10.1175/JPO3130.1](http://dx.doi.org/10.1175/JPO3130.1), iISBN: 0022-3670.
- 781 Mackay, N., J. R. Ledwell, M.-J. Messias, A. C. N. Garabato, J. A. Brearley, A. J. S.
782 Meijers, D. C. Jones, and A. J. Watson, 2018: Diapycnal Mixing in the Southern
783 Ocean Diagnosed Using the DIMES Tracer and Realistic Velocity Fields. *Journal of Geo-*
784 *physical Research: Oceans*, **123** (4), 2615–2634, <https://doi.org/https://doi.org/10.1002/>

785 2017JC013536, URL <https://agupubs.onlinelibrary.wiley.com/doi/abs/10.1002/2017JC013536>,
786 _eprint: <https://agupubs.onlinelibrary.wiley.com/doi/pdf/10.1002/2017JC013536>.

787 MacKinnon, J. A., and Coauthors, 2017: Climate Process Team on Internal Wave–Driven Ocean
788 Mixing. *Bulletin of the American Meteorological Society*, **98** (11), 2429–2454, <https://doi.org/10.1175/BAMS-D-16-0030.1>, URL <http://journals.ametsoc.org/doi/10.1175/BAMS-D-16-0030.1>.
789

790 Marshall, J., C. Hill, L. Perelman, and A. Adcroft, 1997: Hydrostatic, quasi-hydrostatic, and non-
791 hydrostatic ocean modeling. *Journal of Geophysical Research*, **102** (C3), 5733, <https://doi.org/10.1029/96JC02776>, iISBN: 2156-2202.
792

793 Marshall, J., D. Jamous, and J. Nilsson, 1999: Reconciling thermodynamic and dynamic methods
794 of computation of water-mass transformation rates. *Deep-Sea Research Part I: Oceanographic
795 Research Papers*, **46** (4), 545–572, [https://doi.org/10.1016/S0967-0637\(98\)00082-X](https://doi.org/10.1016/S0967-0637(98)00082-X), iISBN:
796 0967-0637.

797 Mashayek, A., R. Ferrari, S. Merrifield, J. R. Ledwell, L. St Laurent, and A. N. Garabato,
798 2017: Topographic enhancement of vertical turbulent mixing in the Southern Ocean. *Nature
799 Communications*, **8**, 14 197, <https://doi.org/10.1038/ncomms14197>, URL <http://www.nature.com/doi/10.1038/ncomms14197>, publisher: Nature Publishing Group.
800

801 McDougall, T. J., and R. Ferrari, 2017: Abyssal Upwelling and Downwelling Driven by Near-
802 Boundary Mixing. *Journal of Physical Oceanography*, **47** (2), 261–283, <https://doi.org/10.1175/JPO-D-16-0082.1>, URL <https://journals.ametsoc.org/doi/full/10.1175/JPO-D-16-0082.1>,
803 publisher: American Meteorological Society.
804

805 McWilliams, J. C., 2016: Submesoscale currents in the ocean. *Proceedings of the Royal Society
806 A: Mathematical, Physical and Engineering Sciences*, **472** (2189), 20160 117, <https://doi.org/10.1098/rspa.2016.0117>, URL <https://royalsocietypublishing.org/doi/10.1098/rspa.2016.0117>,
807 publisher: Royal Society.
808

809 Munk, W. H., 1966: Abyssal recipes. *Deep Sea Research and Oceanographic Abstracts*,
810 **13** (4), 707–730, [https://doi.org/10.1016/0011-7471\(66\)90602-4](https://doi.org/10.1016/0011-7471(66)90602-4), arXiv: cs/9605103 iISBN:
811 1600117471.

- 812 Munk, W. H., and C. Wunsch, 1998: Abyssal Recipes II: energetics of tidal and wind mixing.
813 *Deep-Sea Research Part I: Oceanographic Research Papers*, **45**, 1978–2010.
- 814 Nazarian, R. H., C. M. Burns, S. Legg, M. C. Buijsman, H. Kaur, and
815 B. K. Arbic, 2021: On the Magnitude of Canyon-Induced Mixing. *Journal of*
816 *Geophysical Research: Oceans*, **126** (11), e2021JC017671, [https://doi.org/10.1029/](https://doi.org/10.1029/2021JC017671)
817 [2021JC017671](https://doi.org/10.1029/2021JC017671), URL <https://onlinelibrary.wiley.com/doi/abs/10.1029/2021JC017671>, _eprint:
818 <https://onlinelibrary.wiley.com/doi/pdf/10.1029/2021JC017671>.
- 819 Nikurashin, M., and R. Ferrari, 2009: Radiation and Dissipation of Internal Waves Gener-
820 ated by Geostrophic Motions Impinging on Small-Scale Topography: Theory. *Journal of*
821 *Physical Oceanography*, **40** (5), 1055–1074, <https://doi.org/10.1175/2009JPO4199.1>, URL
822 <https://journals.ametsoc.org/doi/full/10.1175/2009JPO4199.1>.
- 823 Nikurashin, M., and S. Legg, 2011: A Mechanism for Local Dissipation of Internal Tides Generated
824 at Rough Topography. *Journal of Physical Oceanography*, **41** (2), 378–395, [https://doi.org/](https://doi.org/10.1175/2010JPO4522.1)
825 [10.1175/2010JPO4522.1](https://doi.org/10.1175/2010JPO4522.1), URL <http://journals.ametsoc.org/doi/abs/10.1175/2010JPO4522.1>.
- 826 Osborn, T. R., 1980: Estimates of the Local Rate of Vertical Diffusion from Dissipation
827 Measurements. *Journal of Physical Oceanography*, **10** (1), 83–89, [https://doi.org/10.1175/](https://doi.org/10.1175/1520-0485(1980)010<0083:EOTLRO>2.0.CO;2)
828 [1520-0485\(1980\)010<0083:EOTLRO>2.0.CO;2](https://doi.org/10.1175/1520-0485(1980)010<0083:EOTLRO>2.0.CO;2), URL [http://journals.ametsoc.org/doi/abs/10.](http://journals.ametsoc.org/doi/abs/10.1175/1520-0485%281980%29010%3C0083%3AEOTLRO%3E2.0.CO%3B2)
829 [1175/1520-0485%281980%29010%3C0083%3AEOTLRO%3E2.0.CO%3B2](http://journals.ametsoc.org/doi/abs/10.1175/1520-0485%281980%29010%3C0083%3AEOTLRO%3E2.0.CO%3B2).
- 830 Osborn, T. R., and C. S. Cox, 1972: Oceanic fine structure. *Geophysical Fluid Dynamics*, **3** (1),
831 321–345, <https://doi.org/10.1080/03091927208236085>, URL [http://www.tandfonline.com/doi/](http://www.tandfonline.com/doi/abs/10.1080/03091927208236085)
832 [abs/10.1080/03091927208236085](http://www.tandfonline.com/doi/abs/10.1080/03091927208236085).
- 833 Polzin, K., J. Toole, J. R. Ledwell, and R. Schmitt, 1997: Spatial Variability of Turbulent Mix-
834 ing in the Spatial Variability Abyssal Ocean. *Science*, **276** (5309), 93–96, [https://doi.org/10.](https://doi.org/10.1126/science.276.5309.93)
835 [1126/science.276.5309.93](https://doi.org/10.1126/science.276.5309.93), URL <http://www.sciencemag.org/cgi/content/abstract/276/5309/93>,
836 ISBN: 0036-8075.
- 837 Polzin, K. L., 2009: An abyssal recipe. *Ocean Modelling*, **30** (4), 298–309, [https://doi.org/10.](https://doi.org/10.1016/j.ocemod.2009.07.006)
838 [1016/j.ocemod.2009.07.006](https://doi.org/10.1016/j.ocemod.2009.07.006).

839 Polzin, K. L., and T. J. McDougall, 2022: Chapter 7 - Mixing at the ocean's bottom boundary.
840 *Ocean Mixing*, M. Meredith, and A. Naveira Garabato, Eds., Elsevier, 145–180, [https://doi.org/](https://doi.org/10.1016/B978-0-12-821512-8.00014-1)
841 10.1016/B978-0-12-821512-8.00014-1, URL [https://www.sciencedirect.com/science/article/](https://www.sciencedirect.com/science/article/pii/B9780128215128000141)
842 [pii/B9780128215128000141](https://www.sciencedirect.com/science/article/pii/B9780128215128000141).

843 Polzin, K. L., J. M. Toole, R. W. Schmitt, K. L. Polzin, J. M. Toole, and R. W. Schmitt, 1995:
844 Finescale Parameterizations of Turbulent Dissipation. *Journal of Physical Oceanography*, **25** (3),
845 306–328, [https://doi.org/10.1175/1520-0485\(1995\)025<0306:FPOTD>2.0.CO;2](https://doi.org/10.1175/1520-0485(1995)025<0306:FPOTD>2.0.CO;2).

846 Ruan, X., and J. Callies, 2020: Mixing-Driven Mean Flows and Submesoscale Eddies over
847 Mid-Ocean Ridge Flanks and Fracture Zone Canyons. *Journal of Physical Oceanography*,
848 **50** (1), 175–195, <https://doi.org/10.1175/JPO-D-19-0174.1>, URL [https://journals.ametsoc.org/](https://journals.ametsoc.org/view/journals/phoc/50/1/jpo-d-19-0174.1.xml)
849 [view/journals/phoc/50/1/jpo-d-19-0174.1.xml](https://journals.ametsoc.org/view/journals/phoc/50/1/jpo-d-19-0174.1.xml), publisher: American Meteorological Society
850 Section: Journal of Physical Oceanography.

851 Ruan, X., and R. Ferrari, 2021: Diagnosing Diapycnal Mixing from Passive Tracers. *Journal*
852 *of Physical Oceanography*, **51** (3), 757–767, <https://doi.org/10.1175/JPO-D-20-0194.1>, URL
853 <https://journals.ametsoc.org/view/journals/phoc/51/3/JPO-D-20-0194.1.xml>, publisher: Amer-
854 ican Meteorological Society Section: Journal of Physical Oceanography.

855 Simmons, H. L., S. R. Jayne, L. C. St. Laurent, and A. J. Weaver, 2004: Tidally driven mixing
856 in a numerical model of the ocean general circulation. *Ocean Modelling*, **6** (3-4), 245–263,
857 [https://doi.org/10.1016/S1463-5003\(03\)00011-8](https://doi.org/10.1016/S1463-5003(03)00011-8), ISBN: 1463-5003.

858 Spingys, C. P., A. C. N. Garabato, S. Legg, K. L. Polzin, E. P. Abrahamson, C. E. Buck-
859 ingham, A. Forryan, and E. E. Frajka-Williams, 2021: Mixing and Transformation in a
860 Deep Western Boundary Current: A Case Study. *Journal of Physical Oceanography*, **51** (4),
861 1205–1222, <https://doi.org/10.1175/JPO-D-20-0132.1>, URL [https://journals.ametsoc.org/view/](https://journals.ametsoc.org/view/journals/phoc/aop/JPO-D-20-0132.1/JPO-D-20-0132.1.xml)
862 [journals/phoc/aop/JPO-D-20-0132.1/JPO-D-20-0132.1.xml](https://journals.ametsoc.org/view/journals/phoc/aop/JPO-D-20-0132.1/JPO-D-20-0132.1.xml), publisher: American Meteorolog-
863 ical Society Section: Journal of Physical Oceanography.

864 St. Laurent, L., and R. W. Schmitt, 1999: The Contribution of Salt Fingers to Vertical
865 Mixing in the North Atlantic Tracer Release Experiment. *Journal of Physical Oceanog-*
866 *raphy*, **29** (7), 1404–1424, [https://doi.org/10.1175/1520-0485\(1999\)029<1404:TCOSFT>](https://doi.org/10.1175/1520-0485(1999)029<1404:TCOSFT>)

867 2.0.CO;2, URL https://journals.ametsoc.org/view/journals/phoc/29/7/1520-0485_1999_029_
868 [1404_tcosft_2.0.co_2.xml](https://journals.ametsoc.org/view/journals/phoc/29/7/1520-0485_1999_029_1404_tcosft_2.0.co_2.xml), publisher: American Meteorological Society Section: Journal of
869 Physical Oceanography.

870 St. Laurent, L. C., J. M. Toole, and R. W. Schmitt, 2001: Buoyancy Forcing by Turbulence above
871 Rough Topography in the Abyssal Brazil Basin*. *Journal of Physical Oceanography*, **31** (12),
872 3476–3495, [https://doi.org/10.1175/1520-0485\(2001\)031<3476:BFBTAR>2.0.CO;2](https://doi.org/10.1175/1520-0485(2001)031<3476:BFBTAR>2.0.CO;2).

873 Stommel, H., and A. B. Arons, 1959: On the abyssal circulation of the world ocean —
874 II. An idealized model of the circulation pattern and amplitude in oceanic basins. *Deep*
875 *Sea Research (1953)*, **6**, 217–233, [https://doi.org/10.1016/0146-6313\(59\)90075-9](https://doi.org/10.1016/0146-6313(59)90075-9), URL [http:](http://www.sciencedirect.com/science/article/pii/0146631359900759)
876 [//www.sciencedirect.com/science/article/pii/0146631359900759](http://www.sciencedirect.com/science/article/pii/0146631359900759).

877 Sundermeyer, M. A., E. A. Terray, J. R. Ledwell, A. G. Cunningham, P. E. LaRocque, J. Banic,
878 and W. J. Lillycrop, 2007: Three-Dimensional Mapping of Fluorescent Dye Using a Scanning,
879 Depth-Resolving Airborne Lidar. *Journal of Atmospheric and Oceanic Technology*, **24** (6), 1050–
880 1065, <https://doi.org/10.1175/JTECH2027.1>, URL [https://journals.ametsoc.org/view/journals/](https://journals.ametsoc.org/view/journals/atot/24/6/jtech2027_1.xml)
881 [atot/24/6/jtech2027_1.xml](https://journals.ametsoc.org/view/journals/atot/24/6/jtech2027_1.xml), publisher: American Meteorological Society Section: Journal of
882 Atmospheric and Oceanic Technology.

883 Talley, L. D., 2013: Closure of the Global Overturning Circulation Through the Indian, Pacific, and
884 Southern Oceans: Schematics and Transports. *Oceanography*, **26** (1), 80–97, [https://doi.org/10.](https://doi.org/10.5670/oceanog.2013.07)
885 [5670/oceanog.2013.07](https://doi.org/10.5670/oceanog.2013.07), URL [http://apps.webofknowledge.com/full_record.do?product=UA&](http://apps.webofknowledge.com/full_record.do?product=UA&search_mode=GeneralSearch&qid=14&SID=W1jPgX8kkS6brME6NvD&page=1&doc=1)
886 [search_mode=GeneralSearch&qid=14&SID=W1jPgX8kkS6brME6NvD&page=1&doc=1](http://apps.webofknowledge.com/full_record.do?product=UA&search_mode=GeneralSearch&qid=14&SID=W1jPgX8kkS6brME6NvD&page=1&doc=1),
887 arXiv: 1011.1669v3 ISBN: 1042-8275.

888 Taylor, G. I., 1922: Diffusion by Continuous Movements. *Proceedings of the London Mathe-*
889 *matical Society*, **s2-20** (1), 196–212, <https://doi.org/https://doi.org/10.1112/plms/s2-20.1.196>,
890 URL <https://londmathsoc.onlinelibrary.wiley.com/doi/abs/10.1112/plms/s2-20.1.196>, _eprint:
891 <https://londmathsoc.onlinelibrary.wiley.com/doi/pdf/10.1112/plms/s2-20.1.196>.

892 Thorpe, S. A., and G. E. R. Deacon, 1977: Turbulence and mixing in a Scottish Loch.
893 *Philosophical Transactions of the Royal Society of London. Series A, Mathematical and*
894 *Physical Sciences*, **286** (1334), 125–181, <https://doi.org/10.1098/rsta.1977.0112>, URL [https:](https://royalsocietypublishing.org/doi/10.1098/rsta.1977.0112)
895 [//royalsocietypublishing.org/doi/10.1098/rsta.1977.0112](https://royalsocietypublishing.org/doi/10.1098/rsta.1977.0112), publisher: Royal Society.

- 896 Thurnherr, A. M., L. Clément, L. S. Laurent, R. Ferrari, and T. Ijichi, 2020: Transformation
897 and Upwelling of Bottom Water in Fracture Zone Valleys. *Journal of Physical Oceanogra-*
898 *phy*, **50** (3), 715–726, <https://doi.org/10.1175/JPO-D-19-0021.1>, URL <https://journals.ametsoc.org/view/journals/phoc/50/3/jpo-d-19-0021.1.xml>, publisher: American Meteorological Soci-
899 ety Section: Journal of Physical Oceanography.
900
- 901 Thurnherr, A. M., and Coauthors, 2005: Mixing Associated with Sills in a Canyon on the Mid-ocean
902 Ridge Flank*. *Journal of Physical Oceanography*, **35** (8), 1370–1381, <https://doi.org/10.1175/JPO2773.1>, URL <http://journals.ametsoc.org/doi/abs/10.1175/JPO2773.1>.
903
- 904 Tozer, B., D. T. Sandwell, W. H. F. Smith, C. Olson, J. R. Beale, and P. Wes-
905 sel, 2019: Global Bathymetry and Topography at 15 Arc Sec: SRTM15+. *Earth*
906 *and Space Science*, **6** (10), 1847–1864, <https://doi.org/10.1029/2019EA000658>,
907 URL <https://agupubs.onlinelibrary.wiley.com/doi/abs/10.1029/2019EA000658>,
908 [_eprint: https://agupubs.onlinelibrary.wiley.com/doi/pdf/10.1029/2019EA000658](https://agupubs.onlinelibrary.wiley.com/doi/pdf/10.1029/2019EA000658).
- 909 Trossman, D., and Coauthors, 2020: Tracer and observationally-derived constraints on horizontal
910 and diapycnal diffusivities in ocean models. URL [http://www.essoar.org/doi/10.1002/essoar.](http://www.essoar.org/doi/10.1002/essoar.10502123.4)
911 [10502123.4](http://www.essoar.org/doi/10.1002/essoar.10502123.4), archive Location: world Publisher: Earth and Space Science Open Archive Section:
912 Oceanography, <https://doi.org/10.1002/essoar.10502123.4>.
- 913 Tulloch, R., and Coauthors, 2014: Direct Estimate of Lateral Eddy Diffusivity Upstream of
914 Drake Passage. *Journal of Physical Oceanography*, **44** (10), 2593–2616, <https://doi.org/10.1175/JPO-D-13-0120.1>, URL [https://journals.ametsoc.org/view/journals/phoc/44/10/jpo-d-13-0120.](https://journals.ametsoc.org/view/journals/phoc/44/10/jpo-d-13-0120.1.xml)
915 [1.xml](https://journals.ametsoc.org/view/journals/phoc/44/10/jpo-d-13-0120.1.xml), publisher: American Meteorological Society Section: Journal of Physical Oceanography.
916
- 917 Visbeck, M., M. Dengler, T. S. Tanhua, and M. Freund, 2020: Mixing and Upwelling Dy-
918 namics along the Continental Slope off Peru inferred from Tracer Release, Hydrographic and
919 Microstructure Measurements. AGU, URL [https://agu.confex.com/agu/osm20/meetingapp.cgi/](https://agu.confex.com/agu/osm20/meetingapp.cgi/Paper/651229)
920 [Paper/651229](https://agu.confex.com/agu/osm20/meetingapp.cgi/Paper/651229).
- 921 Walin, G., 1982: On the relation between sea-surface heat flow and thermal circulation in the
922 ocean. *Tellus*, **34** (2), 187–195, <https://doi.org/10.3402/tellusa.v34i2.10801>, URL <https://doi.org/10.3402/tellusa.v34i2.10801>.
923

- 924 Waterhouse, A. F., and Coauthors, 2014: Global Patterns of Diapycnal Mixing from Measure-
925 ments of the Turbulent Dissipation Rate. *Journal of Physical Oceanography*, **44** (7), 1854–
926 1872, <https://doi.org/10.1175/JPO-D-13-0104.1>, URL <http://journals.ametsoc.org/doi/abs/10.1175/JPO-D-13-0104.1>, ISBN: 0022-3670.
927
- 928 Waterman, S., A. C. N. Garabato, and K. L. Polzin, 2013: Internal Waves and Turbu-
929 lence in the Antarctic Circumpolar Current. *Journal of Physical Oceanography*, **43** (2),
930 259–282, <https://doi.org/10.1175/JPO-D-11-0194.1>, URL [https://journals.ametsoc.org/view/](https://journals.ametsoc.org/view/journals/phoc/43/2/jpo-d-11-0194.1.xml)
931 [journals/phoc/43/2/jpo-d-11-0194.1.xml](https://journals.ametsoc.org/view/journals/phoc/43/2/jpo-d-11-0194.1.xml), publisher: American Meteorological Society Section:
932 Journal of Physical Oceanography.
- 933 Watson, A. J., J. R. Ledwell, M.-J. Messias, B. A. King, N. Mackay, M. P. Meredith, B. Mills,
934 and A. C. Naveira Garabato, 2013: Rapid cross-density ocean mixing at mid-depths in the
935 Drake Passage measured by tracer release. *Nature*, **501** (7467), 408–411, [https://doi.org/10.1038/](https://doi.org/10.1038/nature12432)
936 [nature12432](https://doi.org/10.1038/nature12432), URL <http://www.nature.com/articles/nature12432>, publisher: Nature Publishing
937 Group.
- 938 Watson, A. J., J. R. Ledwell, D. J. Webb, and C. Wunsch, 1988: Purposefully Released Tracers
939 [and Discussion]. *Philosophical Transactions of the Royal Society of London. Series A, Mathe-*
940 *matical and Physical Sciences*, **325** (1583), 189–200, URL <https://www.jstor.org/stable/38109>,
941 publisher: The Royal Society.
- 942 Wenegrat, J. O., J. Callies, and L. N. Thomas, 2018: Submesoscale Baroclinic Instability in the
943 Bottom Boundary Layer. *Journal of Physical Oceanography*, JPO–D–17–0264.1, [https://doi.org/](https://doi.org/10.1175/JPO-D-17-0264.1)
944 [10.1175/JPO-D-17-0264.1](https://doi.org/10.1175/JPO-D-17-0264.1), URL <http://journals.ametsoc.org/doi/10.1175/JPO-D-17-0264.1>.
- 945 Whalen, C. B., 2021: Best Practices for Comparing Ocean Turbulence Measurements across
946 Spatiotemporal Scales. *Journal of Atmospheric and Oceanic Technology*, **38** (4), 837–841,
947 <https://doi.org/10.1175/JTECH-D-20-0175.1>, URL [https://journals.ametsoc.org/view/journals/](https://journals.ametsoc.org/view/journals/atot/38/4/JTECH-D-20-0175.1.xml)
948 [atot/38/4/JTECH-D-20-0175.1.xml](https://journals.ametsoc.org/view/journals/atot/38/4/JTECH-D-20-0175.1.xml), publisher: American Meteorological Society Section:
949 Journal of Atmospheric and Oceanic Technology.
- 950 Whalen, C. B., C. de Lavergne, A. C. Naveira Garabato, J. M. Klymak, J. A. MacKinnon,
951 and K. L. Sheen, 2020: Internal wave-driven mixing: governing processes and consequences

952 for climate. *Nature Reviews Earth & Environment*, **1 (11)**, 606–621, <https://doi.org/10.1038/>
953 [s43017-020-0097-z](https://doi.org/10.1038/s43017-020-0097-z), URL <https://www.nature.com/articles/s43017-020-0097-z>, number: 11
954 Publisher: Nature Publishing Group.